COUPLED MODE AND FINITE ELEMENT APPROXIMATIONS OF UNDERWATER SOUND PROPAGATION PROBLEMS IN GENERAL STRATIFIED ENVIRONMENTS

G. A. ATHANASSOULIS, K. A. BELIBASSAKIS
Dept. of Naval Arch. and Marine Engineering,
National Technical University of Athens,
15710 Zografos, Greece
mathan@central.ntua.gr
and
D. A. MITSOUDIS[2,3], N. A. KAMPANIS[2], V. A. DOUGALIS[1,2]
[1]Dept. of Mathematics, University of Athens,
15784 Zographou, Greece
doug@math.uoa.gr
[2]Institute of Applied and Computational Mathematics,
FO.R.T.H., P.O. Box 1527, 71110 Heraklion, Greece
[3]Dept. of Applied Mathematics, University of Crete,
71409 Heraklion, Greece

Abstract

We compare the results of a coupled mode method (CCMM) with those of a finite element method (FENL) and also of COUPLE on two test problems of sound propagation and scattering in cylindrically symmetric, underwater, multilayered acoustic waveguides with range–dependent interface topographies. We observe, in general, very good agreement between the results of the three codes. In some cases in which the frequency of the harmonic point source is such that an eigenvalue of the local vertical problem remains small in magnitude and changes sign several times in the vicinity of the interface nonhomogeneity, the discrepancies between the results of the three codes increase, but remain small in absolute terms.

Keywords Underwater acoustics; range-dependent waveguides; comparison of coupled mode and finite element codes.

1 Introduction

Solving numerically the sound propagation and scattering problem in range-dependent marine waveguides is a task of central importance in underwater acoustics. In this paper we consider a cylindrically symmetric environment consisting in part of a water layer overlying a multilayered fluid sediment region that is terminated at a finite depth by a horizontal rigid substrate. The topography of interfaces between the various layers may vary with range and the speed of sound is, in general, depth- and range-dependent. The acoustic field is generated by a harmonic point source located on the axis of symmetry in the water. The precise boundary-value problem that

we consider is stated in Section 2. We solve this problem using and comparing three computational techniques: A consistent coupled mode method (CCMM) developed by Athanassoulis and Belibassakis, a finite element method (FENL) developed by Kampanis, Mitsoudis and Dougalis, and the coupled mode code COUPLE, [1].

As is well-known, the classical normal-mode expansion of the acoustic field in a horizontally stratified medium, [2, 3], has been extended in various directions to provide approximations to the solution of the propagation and scattering problem in range-dependent acoustic waveguides. For a slowly-varying bottom or interface topography the adiabatic mode method proposed by Pierce, [4], approximates the acoustic field by neglecting the interaction between the modes. This approach has been pursued and extended in subsequent works (see *e.g.* Pierce, [5]), in which several types of corrections to the adiabatic approximation have been introduced. In the presence of steeper bottom or interface slopes, coupling between the modes becomes significant. To treat this problem Evans, [6, 1], constructed a coupled-mode model by subdividing the waveguide into a finite number of adjacent columns. Then, the wave field is represented as a normal-mode series within each one of the elements; the coefficients are obtained by matching the expansions at the inter-element vertical interfaces. The main feature of this model, and of the widely used associated code COUPLE, [1], is the full coupling between the modes and the satisfactory handling of the backscattering effect. However, approximating the various continuous functions of the problem by piecewise constants usually requires a large number of steps, since the horizontal staircase step should be small enough for accuracy purposes.

Other coupled-mode approaches for treating irregular bottom or interface topographies have been developed, for example, by Rutherford and Hawker, [7], Brekhovskikh and Godin, [8], Fawcett, [9], Chiu *et al.*, [10], and Godin, [11], with the following issue in mind: It is well known, [7, 11], that the series of standard local vertical modes converges very slowly, since at a rigid bottom (or at a penetrable interface) these modes satisfy an incorrect Neumann boundary condition (transmission condition), wherein the normal derivative operator $\frac{\partial}{\partial n}$ is replaced by the derivative $\frac{\partial}{\partial z}$ in the vertical direction. In the cited papers, additional terms have been introduced in the series to handle this inconsistency of the local vertical modes at nonhorizontal interfaces or bottom boundaries. The Consistent Coupled Mode Method (CCMM) used in this paper (*cf.* also [12]), belongs to this category of coupled mode models. It employs an enhanced local mode representation of the field in the vicinity of the variable topography by including an additional local field function, the 'sloping bottom (interface) mode', whose range-dependent coefficient provides an extra degree of freedom that is used to correct the previously mentioned inconsistency of the local vertical modes. This series solution in the nonhomogeneous part of the waveguide (intermediate field) is appropriately truncated and coupled, via a variational equation, with the near- and far-field standard normal mode representation of the field in the respective, homogeneous, parts of the waveguide. CCMM is described in detail in Section 3 of the paper.

Finite element methods form a class of direct discretization techniques that is designed to solve efficiently boundary-value problems that have discontinuous coefficients and/or are posed

in domains with complex geometry, such as range-dependent waveguides. For an overview of earlier finite element methods in underwater acoustics we refer the reader to the survey of Buckingham, [13], which also includes a wealth of information and commentary on other types of computational models. In the paper at hand we use the code FENL, [14], (see Section 4), which implements a standard Galerkin discretization of the Helmholtz equation using continuous, piecewise linear functions on a triangulation of the computational domain. At an artificial outflow boundary far from the source the finite element solver is coupled to a nonlocal, nonreflecting Dirichlet-to-Neumann (DtN) boundary condition that uses the normal-mode representation of the outgoing solution in the homogeneous far-field portion of the waveguide. This type of condition, discretized properly, cooperates well with an interior finite element solver and allows for the perfect absorption of outgoing radiation in the waveguide under consideration. It was introduced in finite element approximations of underwater acoustics problems by Fix and Marin, [15], and was analyzed in detail by Goldstein, [16]; see also Keller and Givoli, [17], for a wider class of applications. For error estimates, *cf.* [16, 18]. At an inner artificial boundary in the near field we used, in general, the CCMM-computed field as a nonhomogeneous Dirichlet boundary condition for the FENL. Thus, the FENL code is not self-contained as it stands, and depends on modal data at the inner boundary. (The use of a modal starter causes apparent resonances at some frequencies, as discussed at the end of Section 5.) The resulting large, sparse, indefinite, complex linear systems of finite element equations are solved by preconditioned iterative methods based on the conjugate-gradient type/non symmetric Lanczos schemes of the QMR method of Freund, [19]. For a detailed experimental study of the application of such iterative methods on discretizations of the Helmholtz equation such as the ones considered here, *cf.* Mitsoudis, [18].

We performed many numerical experiments and compared in some detail the results of the three codes on two test problems with one lossless sediment layer separated from the water column by a hill- and a trench-like interface, respectively. In the near- and far-field parts of the waveguide we assume that the interface is horizontal and lies at the same depth. We believe that there is a need for comparing and validating the results of codes that use different methods for the same mathematical model on interesting benchmark problems. This has been done extensively in the case of the Parabolic Equation in 2D (see *e.g.* Buckingham, [13], for a convenient list of references), but a similar comprehensive study is still lacking for Helmholtz solvers in underwater acoustic range-dependent waveguides. (There are, of course, many numerical results for the benchmark pressure-release wedge, [13], for which a special, exact solution is available, [20]. In addition, many smaller scale comparisons of pairs of particular codes can be found in the literature. We have made no systematic search but we mention, for example, Fawcett,[9], in which a comparison between the results of a coupled method and a boundary element method is recorded, and Ref.[21], where an earlier version of FENL was compared to MODE4, a coupled mode method written by Taroudakis, [22, 23]).

In our numerical experiments, presented in Section 5, we found that, in general, the results of the three codes were in very good agreement. We noticed larger discrepancies at some

source frequencies, for which some eigenvalue $k_n^2(r)$ of the local, depth eigenvalue problem, that defines the local modes, changed sign several times and remained small in magnitude in the neighborhood of the nonhomogeneity in the interface topography. In the near- and far-field parts of the waveguide the domain is assumed homogeneous and the eigenvalues are constant and are associated either with a propagating mode, if they are positive, or with an evanescent one if they are negative. (For the source frequencies that we used, the eigenvalues in the homogeneous parts of the waveguide were nonzero.) As the interface is perturbed, forming in our case a hill or a trench supported on a bounded interval I in range, some eigenvalue of small magnitude may, often repeatedly, change sign in I before returning to its constant, nonzero value when the interface becomes again horizontal for large enough r. In such a case the corresponding mode is 'confused', changing its character repeatedly in I from propagating to evanescent and vice versa. (A source frequency for which this happens may be thought of as a 'multiple cut-off' frequency for the particular mode.)

It is not unreasonable to expect that schemes that use modal expansions may experience computational instabilities near such frequencies. If the interface was horizontal, the modal amplitude functions $P_n(r)$ (*cf.* Eq. (28)) would be Hankel functions with argument $k_n r$, which are singular if $k_n = 0$. Hence, it is of interest to study how this multiple cut-off phenomenon affects coupled mode schemes in cases of variable interface topography and to compare their results with those of a finite element scheme. In our numerical experiments, as we document in detail in Section 5, we observed indeed somewhat larger discrepancies between the results of the three codes in some cases of multiple cut-off frequencies, compared with the discrepancies at 'regular' source frequencies. However, these discrepancies were, in general, small in absolute terms. This is of some significance, since computing the sound field in such 'ideal' waveguides in the case of multiple cut-off frequencies, is not easy. Of course, it may be argued that the lack of material absorption (attenuation) in the medium, combined with the Neumann bottom boundary condition at a finite depth, make our test examples rather unrealistic for the underwater acoustic waveguide application, where this multiple cut-off phenomenon is not expected to occur. This is indeed the case in practice but examples of ideal waveguides are still important as hard benchmarks to test one's codes on.

2 The boundary–value problem

We consider a cylindrically symmetric, range-dependent environment, which consists of a water layer confined between a pressure-release surface and a multilayered fluid sediment bottom region of irregular shape, terminated by a perfectly rigid substrate located at a depth H below the free surface; see Figure 1. In the sequel, for simplicity, we shall assume that we have only one sediment layer.

A cylindrical co-ordinate system (r, z, θ) is introduced with origin at the free-surface, the vertical axis z being positive downwards. The wave field is excited by a harmonic point source, located at $r = 0$ at an arbitrary depth z_0. It is assumed that the bathymetry is described by a

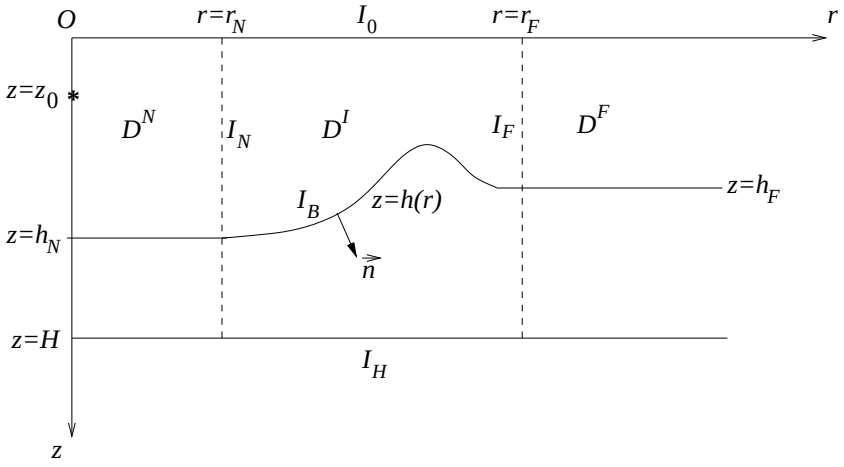

Figure 1: Geometric configuration and basic notation. The point source is denoted by an asterisk.

smooth function (C^2 will suffice) of the form:

$$h(r) = \begin{cases} h_N & , \quad r \le r_N \\ h_I(r) & , \quad r_N \le r \le r_F \\ h_F & , \quad r \ge r_F, \end{cases} \tag{1}$$

where h_N and h_F are constants. (We usually drop the subscript I of h_I in $[r_N, r_F]$.) The domain D of the problem consists of three parts: (i) The near-field, bounded subdomain D^N ($0 < r < r_N$), (ii) the intermediate, bounded subdomain D^I with the range-dependent part of the interface, and (iii) the far-field, unbounded subdomain D^F ($r > r_F$). The vertical artificial interface between D^N and D^I is denoted by I_N, and the one between D^I and D^F by I_F. The parts of the free surface, the water–sediment interface, and the hard bottom surface lying between the two cylinders $r = r_N$ and $r = r_F$ are denoted by I_0, I_B and I_H, respectively. In the sequel we shall sometimes use the generic symbol D^* to denote any one of the three subdomains D^N, D^I, D^F. That is, $* \in \{N, I, F\}$. The sound speed is considered to be range-independent in D^N and D^F (*i.e.* $c = c^N(z)$ and $c = c^F(z)$, respectively), and varies smoothly from its near-field to its far-field value within each layer in the intermediate subdomain D^I. The density ρ is assumed to be constant within each layer and is equal to ρ_1 in the water and ρ_2 ($\rho_2 > \rho_1$) in the sediment layer.

The formulation of the acoustic propagation and scattering problem in this environment is classical, [2, 3]. The acoustic field satisfies in each layer the Helmholtz equation

$$\Delta p(r,z) + k^2(r,z)\, p(r,z) = -\frac{1}{2\pi}\, \frac{\delta(r)}{r}\, \delta(z - z_0), \tag{2}$$

where $k\,(r,z) = \omega / c\,(r,z)$ is the wavenumber and $\Delta p = p_{zz} + p_{rr} + \frac{1}{r}\, p_r$. The p.d.e. (2) is supplemented by the boundary conditions

$$p(r,0) \quad = \quad 0, \quad r > 0 \tag{3}$$

$$\frac{\partial p}{\partial z}(r,H) \;=\; 0, \quad r>0, \tag{4}$$

the interface conditions

$$p \text{ continuous across } z=h(r), \tag{5}$$

$$\frac{1}{\rho_1}\frac{\partial p(r,h(r)^-)}{\partial n}=\frac{1}{\rho_2}\frac{\partial p(r,h(r)^+)}{\partial n}, \quad r>0, \tag{6}$$

and the radiation condition

$$p(r,z) \text{ behaves like an outgoing cylindrical wave as } r\to\infty. \tag{7}$$

The normal derivative on I_B, appearing in Eq. (6), is given by

$$\frac{\partial}{\partial n}=\frac{\left(\frac{\partial}{\partial z}-h'(r)\frac{\partial}{\partial r}\right)}{\sqrt{1+\left(h'(r)\right)^2}}, \tag{8}$$

where $h'=\frac{dh}{dr}$, *i.e.* is the outward normal of the water layer.

3 A Consistent Coupled Mode Method

3.1 Formulation of the transmission problem

The boundary-value problem (2)–(7) can be reformulated as a transmission problem in the intermediate, bounded subdomain D^I with the aid of the following general, normal-mode representations of the acoustic field in the near- and far-field subdomains D^N and D^F, respectively (see, *e.g.*, Jensen *et al.*, [2]):
Near field:

$$p^N=\frac{i}{4\rho_1}\sum_{n=1}^{\infty}Z_n^N(z_0)\,Z_n^N(z)\,H_0^{(1)}\left(k_n^N r\right)+\sum_{n=1}^{\infty}C_n^N\,Z_n^N(z)\,J_0\left(k_n^N r\right), \quad (r,z)\in D^N. \tag{9}$$

Far field:

$$p^F=\sum_{n=1}^{\infty}C_n^F\,Z_n^F(z)\,H_0^{(1)}\left(k_n^F r\right), \quad (r,z)\in D^F. \tag{10}$$

In formulas (9) and (10) the functions $Z_n^N(z)$, $Z_n^F(z)$ and the numbers k_n^N, k_n^F, $n\in\mathbb{N}$, satisfy the Sturm-Liouville eigenvalue problems:

$$\frac{d^2Z_n^*(z)}{dz^2}+\left(\frac{\omega^2}{\left(c^*\right)^2}-\left(k_n^*\right)^2\right)Z_n^*(z)=0, \quad 0\le z<h_*, h_*<z\le H, \tag{11}$$

$$Z_n^*(0)=0, \tag{12}$$

$$\frac{dZ_n^*(H)}{dz}=0, \tag{13}$$

$$Z_n\left(h_*^-\right)=Z_n\left(h_*^+\right), \tag{14}$$

$$\frac{1}{\rho_1}\frac{\partial Z_n\left(h_*^-\right)}{\partial z}=\frac{1}{\rho_2}\frac{\partial Z_n\left(h_*^+\right)}{\partial z}, \tag{15}$$

where the asterisk $*$ is N or F, respectively. Here, as usual, we put $k_n^* = \sqrt{(k_n^*)^2}$ if $(k_n^*)^2 \geq 0$, and $k_n^* = i\sqrt{-(k_n^*)^2}$ if $(k_n^*)^2 < 0$. We assume that the problem (11)–(15) is such that $k_n^* \neq 0$ for all n. The function p^N satisfies Eqs. (2)–(6) in D^N, while p^F satisfies Eqs. (3)–(7) and the homogeneous analog of (2) in D^F. In case D^N and D^F consist of two homogeneous layers of thicknesses $h_1 = h_*$ and $h_2 = H - h_*$, with corresponding sound speeds c_1 and c_2, the eigenvalues $k_n^2 = (k_n^*)^2$ may be obtained, [3], as the roots of the equation

$$\frac{h_2}{h_1}\,\frac{\rho_2}{\rho_1}\,\frac{\Lambda_1(\lambda)}{\Lambda_2(\lambda)}\,\cos\Lambda_1\,\cos\Lambda_2 = \sin\Lambda_1\,\sin\Lambda_2, \tag{16}$$

where

$$\Lambda_1\left(k_n^2\right) = h_1\sqrt{(\omega/c_1)^2 - k_n^2}, \quad \text{and} \quad \Lambda_2\left(k_n^2\right) = h_2\sqrt{(\omega/c_2)^2 - k_n^2}. \tag{17}$$

We may now formulate the transmission problem $P_T\left(D^I,\, k(r,z)\right)$ in D^I as follows: Given $k(r,z) = \omega/c(r,z)$ and the representations (9) and (10) of the pressure field in D^N and D^F, find the coefficients $\left\{C_n^N\right\}_{n\in\mathbb{N}}$ of p^N and $\left\{C_n^F\right\}_{n\in\mathbb{N}}$ of p^F, and the field $p^I(r,z)$ in D^I so that

$$\Delta p^I + k^2(r,z)p^I = 0, \quad (r,z) \in D^I. \tag{18}$$

For $r_N \leq r \leq r_F$ we impose the boundary conditions

$$p^I(r,0) = 0, \tag{19}$$

$$\frac{\partial p^I(r,H)}{\partial z} = 0, \tag{20}$$

and the interface conditions

$$p^I\left(r,h(r)^-\right) = p^I\left(r,h(r)^+\right), \tag{21}$$

$$\frac{1}{\rho_1}\,\frac{\partial p^I\left(r,h(r)^-\right)}{\partial n} = \frac{1}{\rho_2}\,\frac{\partial p^I\left(r,h(r)^+\right)}{\partial n}. \tag{22}$$

In addition, the following matching conditions should hold on I_N and I_F:

$$p^I = p^N, \quad \frac{\partial p^I}{\partial r} = \frac{\partial p^N}{\partial r} \quad \text{on } I_N, \tag{23}$$

$$p^I = p^F, \quad \frac{\partial p^I}{\partial r} = \frac{\partial p^F}{\partial r} \quad \text{on } I_F. \tag{24}$$

3.2 Variational formulation

In order to state a variational formulation of the transmission problem $P_T\left(D^I,\, k(r,z)\right)$, we consider the functional

$$F\left(p^I, \left\{C_n^N\right\}_{n\in\mathbb{N}}, \left\{C_n^F\right\}_{n\in\mathbb{N}}\right) = \sum_{\ell=1}^{2}\left[\frac{1}{2\rho_\ell}\int_{D_\ell^I}\left\{\left(\nabla p^I\right)^2 - k^2\left(p^I\right)^2\right\}dV\right.$$

$$\left. + \frac{1}{\rho_\ell}\int_{I_\ell^N}\left(p^I - \frac{1}{2}p^N\right)\frac{\partial p^N}{\partial r}\,dS - \frac{1}{\rho_\ell}\int\limits_{I_\ell^F}\left(p^I - \frac{1}{2}p^F\right)\frac{\partial p^F}{\partial r}\,dS\right]$$

$$- \frac{1}{2\rho_1}\sum_{n=1}^{\infty} C_n^N Z_n^N(z_0), \tag{25}$$

where the arguments of the functional F are the continuously distributed values of the function $p^I(r,z)$ in D^I, essentially satisfying $p^I(r,0) = 0$ and $p^I(r,h(r)^-) = p^I(r,h(r)^+)$, and the sets of coefficients $\left\{C_n^N\right\}_{n\in\mathbb{N}}$ and $\left\{C_n^F\right\}_{n\in\mathbb{N}}$ appearing in the representations of p^N and p^F, respectively, and D_ℓ^I, I_ℓ^N, I_ℓ^F, $\ell = 1,2$, are the parts of D^I, I^N, I^F in the water and the sediment, respectively. The variational principle governing the variational formulation of the problem $P_T\left(D^I,\ k(r,z)\right)$ can be now stated as follows, [22]: The functions $p^I(r,z)$, and $p^N\left(r,z;\left\{C_n^N\right\}_{n\in\mathbb{N}}\right)$, $p^F\left(r,z;\left\{C_n^F\right\}_{n\in\mathbb{N}}\right)$, of the form given by (9), (10), constitute a solution of the problem $P_T\left(D^I,\ k(r,z)\right)$ if and only if they render the functional F stationary, *i.e.* they satisfy

$$\delta F\left(p^I,\ \left\{C_n^N\right\}_{n\in\mathbb{N}},\ \left\{C_n^F\right\}_{n\in\mathbb{N}}\right) = 0. \tag{26}$$

Indeed, by calculating the first variation δF of the functional (25) and using Green's theorem, we observe that the variational equation (26) takes the form,

$$\begin{aligned}
\delta F \;=\; & \sum_{\ell=1}^{2} \frac{1}{\rho_\ell}\left[-\int_{D_\ell^I}\left(\Delta p^I + k^2 p^I\right)\,\delta p^I\,dV + \right.\\
+\; & \int_{I_\ell^N}\left(\frac{\partial p^N}{\partial r} - \frac{\partial p^I}{\partial r}\right)\delta p^I\,dS + \int_{I_\ell^N}\left(p^I - p^N\right)\frac{\partial}{\partial r}\left(\delta p^N\right)\,dS\\
+\; & \left.\int_{I_\ell^F}\left(\frac{\partial p^F}{\partial r} - \frac{\partial p^I}{\partial r}\right)\delta p^I\,dS - \int_{I_\ell^F}\left(p^I - p^F\right)\,\frac{\partial}{\partial r}\left(\delta p^F\right)\,dS\right] +\\
+\; & \frac{1}{\rho_2}\int_{I_H}\frac{\partial p^I}{\partial n}\,\delta p^I\,dS + \frac{1}{\rho_1}\int_{I_0}\frac{\partial p^I}{\partial n}\,\delta p^I\,dS\\
+\; & \int_{I_B}\left(\frac{1}{\rho_1}\frac{\partial p^I(r,h(r)^-)}{\partial n} - \frac{1}{\rho_2}\frac{\partial p^I(r,h(r)^+)}{\partial n}\right)\delta p^I\,dS = 0.
\end{aligned} \tag{27}$$

Using standard arguments of the calculus of variations (*e.g.*, Gelfand and Fomin, [24], or Rectorys, [25]), one may establish the validity of (27).

The usefulness of the above variational principle hinges on the fact that it gives one the freedom to choose any particular admissible representation for the unknown pressure field p^I in D^I. In this way, a variety of possible methods for the numerical solution of the problem can be constructed. One possible such choice, based on local-mode series, and enabling the consistent treatment of range-dependent problems involving general bathymetry, will be presented in the next subsection.

3.3 The enhanced local-mode representation

For simplicity, in this section the pressure field p^I in the indermediate subdomain D^I is simply denoted p. The standard local-mode representation of p is usually written (Pierce, [4], Fawcett, [9]), as

$$p(r,z) = \sum_{n=1}^{\infty} P_n(r)\,Z_n(z;r). \tag{28}$$

In Eq. (28) the functions $Z_n(z;r)$, $n \in \mathbb{N}$, are the eigenfunctions of the following local, vertical (depth) eigenvalue problem, posed for each $r > 0$:

$$\frac{\partial^2 Z_n(z;r)}{\partial z^2} + \left(k^2(r,z) - k_n^2(r)\right) Z_n(z;r) = 0, \quad 0 \le z < h(r), h(r) < z \le H, \tag{29}$$

$$Z_n(0;r) = 0, \tag{30}$$

$$\frac{\partial Z_n(H;r)}{\partial z} = 0, \tag{31}$$

with the interface conditions

$$Z_n\left(h(r)^-;r\right) = Z_n\left(h(r)^+;r\right), \tag{32}$$

$$\left[\frac{\partial Z_n}{\partial z}\right]_{z=h(r)} = 0, \tag{33}$$

where for a function $\phi = \phi(z)$ we define

$$[\phi]_{z=h(r)} := \frac{1}{\rho_1}\,\phi\left(h(r)^-\right) - \frac{1}{\rho_2}\,\phi\left(h(r)^+\right). \tag{34}$$

For each $r > 0$, in the series expansion (28) a finite number of terms corresponding to the real eigenvalues ($k_n^2 > 0$, $n \le N_p$), are the *propagating modes*, while the rest of the terms, corresponding to imaginary eigenvalues ($k_n^2 < 0$, $n > N_p$), are the *evanescent modes*.

In Eq. (28) $P_n(r)$ may be thought as the coefficients of a generalized Fourier expansion of $p(r,z)$ with respect to the local basis $\{Z_n(z;r)\}_{n\in\mathbb{N}}$. The function $P_n(r)$ is called the (complex) amplitude of the n-th mode. Analytical and numerical evidence shows (see *e.g.* [11, 12]) that

$$|P_n(r)| = O\left(n^{-2}\right), \quad n \to \infty,$$

for $r \in [r_N, r_F]$, which implies a slow rate of convergence for the series (28). This is due to the fact, observed *e.g.* by Fawcett, [9], that the jump condition (33) is incompatible with the correct interface condition (22), when $h'(r) \neq 0$.

In the present paper, we propose an easily implemented extension of the representation (28), which corrects this deficiency and provides significant acceleration of convergence for the series (28). The main idea behind the new representation is to introduce a specific field element $g(r,z)$, such that the difference

$$p_R(r,z) = p(r,z) - g(r,z) \tag{35}$$

satisfies exactly the same boundary and interface conditions as the eigenfunctions $Z_n(z;r)$, *i.e.*

$$p_R(r,0) = 0, \tag{36}$$

$$\frac{\partial p_R(r,H)}{\partial z} = 0, \tag{37}$$

$$p_R\left(r,h(r)^-\right) = p_R\left(r,h(r)^+\right), \tag{38}$$

$$\left[\frac{\partial p_R}{\partial z}\right]_{z=h(r)} = 0. \tag{39}$$

Then, if the 'residual' field $p_R(r,z)$ is expanded in terms of the basis $\{Z_n(z;r)\}_{n\in\mathbb{N}}$, namely if

$$p_R(r,z) = p(r,z) - g(r,z) = \sum_{n=1}^{\infty} P_n(r)\, Z_n(z;r), \tag{40}$$

(where for simplicity of notation, we denote again by $P_n(r)$ the amplitude of the n-th mode of p_R), it is expected that the latter series will exhibit much better convergence properties. To construct such a function $g(r,z)$ we put

$$g(r,z) = P_0(r)\, Z_0(z;r), \tag{41}$$

where

$$P_0(r) = \left[\frac{\partial p}{\partial z}\right]_{z=h(r)}, \tag{42}$$

and $Z_0(z;r)$ is sufficiently smooth for $0 \le z \le h(r)$, and satisfies the conditions

$$Z_0\,(0;\ r) = 0, \tag{43}$$

$$\frac{\partial^2 Z_0(0;\ r)}{\partial z^2} = 0, \tag{44}$$

$$\frac{\partial Z_0\,(H;\ r)}{\partial z} = 0, \tag{45}$$

$$Z_0\left(h(r)^-;r\right) = Z_0\left(h(r)^+;r\right), \tag{46}$$

$$\left[\frac{\partial Z_0}{\partial z}\right]_{z=h(r)} = 1, \tag{47}$$

for each $r \in [r_N,\ r_F]$. A specific, convenient form of the function $Z_0(z;r)$ is given by

$$Z_0(z;r) = \begin{cases} \rho_1\, h(r)\left[\left(\frac{z}{h(r)}\right)^4 - \left(\frac{z}{h(r)}\right)^3\right], & 0 < z < h(r) \\ 0, & h(r) < z < H \end{cases}. \tag{48}$$

Other choices are also possible. The condition (47), in conjunction with Eqs. (41) and (42), implies that

$$\left[\frac{\partial p_R}{\partial z}\right]_{z=h(r)} = \left[\frac{\partial p}{\partial z}\right]_{z=h(r)} - \left[\frac{\partial g}{\partial z}\right]_{z=h(r)} = 0. \tag{49}$$

The function $P_0(r)$ can be interpreted as an additional degree of freedom, accounting for the nonhomogeneity in the jump of $1/\rho$ times the vertical derivative caused by the sloping interface. However, Eq. (42) cannot be used for the direct calculation of $P_0(r)$, since $p(r,z)$ is not known a priori. The function $P_0(r)$ will be found, along with all other amplitude functions $P_n(r)$, $n \in \mathbb{N}$, during the solution procedure. By substituting Eq. (41) into Eq. (40), we obtain the following, enhanced local-mode representation in the range-dependent subdomain D^I:

$$p(r,z) = P_0(r)\, Z_0(z;r) + \sum_{n=1}^{\infty} P_n(r)\, Z_n(z;r) = \sum_{n=0}^{\infty} P_n(r)\, Z_n(z;r). \tag{50}$$

The additional term $P_0(r)\, Z_0(z;r)$, included in the right-hand side of (50), will be called the *sloping interface mode*. An important consequence of the introduction of this mode, as numerical

evidence, [12], shows, is that the coefficients in the enhanced local-mode series exhibit a faster rate of decay, namely are such that

$$|P_n| = O\left(n^{-4}\right), \quad \text{as} \quad n \to \infty,$$

which, implies that much fewer terms of the series need be retained in order to give accurate results in practice.

3.4 The coupled-mode system

If we assume that $p^I(r,z)$ is represented by the enhanced local-mode series (50), the functional $F\left(p^I, \{C_n^N\}_{n\in\mathbb{N}}, \{C_n^F\}_{n\in\mathbb{N}}\right)$, given by Eq. (25), is transformed to an equivalent one of the form

$$F = F\left(\{P_n(r)\}_{n\geq 0}, \{C_n^N\}_{n\in\mathbb{N}}, \{C_n^F\}_{n\in\mathbb{N}}\right),$$

implying that the degrees of freedom of the system associated with the admissible pressure field $p^I(r,z)$ in D^I are the modal amplitudes $P_n(r)$, $r_N < r < r_F$, $n = 0, 1, \ldots$. Associated with the vertical interfaces I_N and I_F are the degrees of freedom $\{P_n(r_N)\}_{n=1,2,\ldots}$ and $\{P_n(r_F)\}_{n=1,2,\ldots}$ of the amplitude values at the left-hand endpoint $r = r_N$, and at the right-hand endpoint $r = r_F$, respectively, as well as the sets of coefficients $\{C_n^N, n = 1, 2, \ldots\}$ and $\{C_n^F, n = 1, 2, \ldots\}$. For the sloping interface mode amplitude $P_0(r)$ we impose the end conditions

$$P_0(r_N) = P_0(r_F) = 0, \text{ and } P_0'(r_N) = P_0'(r_F) = 0, \tag{51}$$

taking into account the smoothness of $h(r)$.

Using a different (equivalent) set of degrees of freedom of the system in the variational principle leads to a different (equivalent) set of equations for the transmission problem $P_T\left(D^I, k(r,z)\right)$. First, assuming that all the variations, except δp^I in $D^I \cup I_B$, are kept zero, we obtain

$$-\sum_{\ell=1}^{2}\left[\frac{1}{\rho_\ell}\int_{D_\ell^I}\left(\Delta p^I + k^2 p^I\right)\,\delta p^I\,dV\right] + \int_{I_B}\left[\frac{\partial p^I}{\partial n}\right]_{z=h(r)}\delta p^I\,dS = 0, \tag{52}$$

from which there formally follows that

$$\sum_{m=0}^{\infty}\int_{r_N}^{r_F}\delta P_m(r)\cdot\left(\sum_{n=0}^{\infty}a_{mn}(r)\,\frac{d^2P_n(r)}{dr^2} + b_{mn}(r)\,\frac{dP_n(r)}{dr} + c_{mn}(r)\,P_n(r)\right)r\,dr = 0, \tag{53}$$

where the coefficients $a_{mn}(r)$, $b_{mn}(r)$, $c_{mn}(r)$ are given, for m, $n \geq 0$, by

$$\begin{aligned}
a_{mn}(r) &= \langle Z_n, Z_m\rangle, &(54)\\
b_{mn}(r) &= (1/r)\,\langle Z_n, Z_m\rangle + 2\,\langle \partial Z_n/\partial r, Z_m\rangle \\
&+ h'(r)\left(\frac{1}{\rho_1} - \frac{1}{\rho_2}\right) Z_n\left(h(r);r\right)\,Z_m\left(h(r);r\right), &(55)\\
c_{mn}(r) &= \left\langle \frac{1}{r}\frac{\partial Z_n}{\partial r} + \frac{\partial^2 Z_n}{\partial r^2} + \frac{\partial^2 Z_n}{\partial z^2} + k^2 Z_n, Z_m\right\rangle - \delta_{0n}\,Z_m(h(r);r) \\
&+ h'(r)\left(\frac{1}{\rho_1}\frac{\partial Z_n\left(h(r)^-;0\right)}{\partial r} - \frac{1}{\rho_2}\frac{\partial Z_n\left(h(r)^+;r\right)}{\partial r}\right) Z_m\left(h(r);r\right), &(56)
\end{aligned}$$

where by $\langle \cdot, \cdot \rangle$ we denote the inner product

$$\langle f, g \rangle = \frac{1}{\rho_1} \int_0^h f(z)\, g(z)\, dz + \frac{1}{\rho_2} \int_h^H f(z)\, g(z)\, dz, \tag{57}$$

with respect to which the set $\{Z_n\}_{n \geq 1}$ is orthonormal. Since $\delta P_m(r)$, $m = 0, 1, 2, 3, \ldots$, are assumed arbitrary, independent variations, Eq. (53) is equivalent to the following infinite system of second order ordinary differential equations:

$$\sum_{n=0}^{\infty} a_{mn}(r)\, \frac{d^2 P_n(r)}{dr^2} + b_{mn}(r)\, \frac{dP_n(r)}{dr} + c_{mn}(r)\, P_n(r) = 0, \quad r_N < r < r_F, \quad m = 0, 1, 2, \ldots, \tag{58}$$

which will be called the *consistent coupled-mode system of horizontal equations*.

The boundary conditions for this system may be derived again using the variational equation (27) and taking appropriate variations. The resulting equations are equivalent to (23) and (24). First, in view of the series representation (9) of p^N, and taking into account (50), we may rewrite the boundary conditions (23) in the form

$$P_n(r_N) = C_n^N J_0\left(k_n^N r_N\right) + \frac{i}{4\rho_1}\, Z_n^N(z_0)\, H_0^{(1)}\left(k_n^N r_N\right), \quad n = 1, 2, 3, \ldots, \tag{59}$$

$$P_n'(r_N) = -\frac{i}{4\rho_1}\, k_n^N\, Z_n^N(z_0)\, H_1^{(1)}\left(k_n^N r_N\right) - C_n^N k_n^N J_1\left(k_n^N r_N\right), \quad n = 1, 2, 3, \ldots. \tag{60}$$

By following the same procedure, we may derive from (23) a similar set of boundary conditions at the right-hand endpoint $r = r_F$

$$P_n(r_F) - C_n^F\, H_0^{(1)}\left(k_n^F r_F\right) = 0, \qquad n = 1, 2, 3, \ldots, \tag{61}$$

$$P_n'(r_F) + k_n^F\, H_1^{(1)}\left(k_n^F r_F\right)\, C_n^F = 0, \qquad n = 1, 2, 3, \ldots. \tag{62}$$

Recapitulating the above results, we see that the solution p of the transmission problem $P_T\left(D^I,\ k(r,z)\right)$ is represented by the series (50), where the amplitudes P_n, $n \geq 0$ satisfy the infinite system of o.d.e's (58) in $r_N < r < r_F$, with coefficients given by the relations (54)–(56). This system is supplemented by the boundary conditions

$$P_0(r_N) = P_0(r_F) = 0, \tag{63}$$

$$P_0'(r_N) = P_0'(r_F) = 0, \tag{64}$$

$$P_n'(r_N) + A_n P_n(r_N) = B_n, \quad n = 1, 2, 3, \ldots \tag{65}$$

$$P_n'(r_F) + D_n P_n'(r_F) = 0, \quad n = 1, 2, 3, \ldots, \tag{66}$$

where the coefficients A_n, B_n, D_n are given, for $n = 1, 2, 3, \ldots$, by the relations

$$A_n = \frac{k_n^N J_1\left(k_n^N r_N\right)}{J_0\left(k_n^N r_N\right)}, \tag{67}$$

$$B_n = \frac{-Z_n^N(z_0)}{2\pi\rho_1 r_N J_0\left(k_n^N r_N\right)}, \tag{68}$$

$$D_n = \frac{k_n^F H_1^{(1)}\left(k_n^F r_F\right)}{H_0^{(1)}\left(k_n^F r_F\right)}. \tag{69}$$

The coefficients C_n^N, C_n^F of the near and far-field expansion are then given by

$$C_n^N = \left[P_n(r_N) - \frac{i}{4} Z_n^N(z_0)\, H_0^{(1)}\left(k_n^N r_N\right)\right] / J_0\left(k_n^N r_N\right), \quad n = 1, 2, 3, \ldots, \tag{70}$$

$$C_n^F = P_n(r_F) / H_0^{(1)}\left(k_n^F r_F\right), \qquad n = 1, 2, 3, \ldots. \tag{71}$$

Remarks:

1. Despite of the coupling between the differential equations (58), the boundary conditions (63)–(66) are uncoupled.

2. Under the smoothness assumption for the depth function $h(r)$, all the coefficients $a_{mn}(r)$, $b_{mn}(r)$, $c_{mn}(r)$ of the system (58) are continuous functions of r and can be calculated in terms of $Z_0(z;r)$ and $\{Z_n(z;r)\}_{n\in\mathbb{N}}$.

3. Discontinuities of $h(r)$, $h'(r)$, and $h''(r)$ can also be treated by introducing an appropriate domain decomposition with matching boundaries/interfaces at the points of discontinuities.

3.5 Implementation of CCMM

The derivation of the Consistent-Couple Mode Method (CCMM) is based on truncating the local-mode series (50) to include only a finite number of terms (modes), namely the sloping-interface mode, the propagating modes and a number of evanescent modes. We write then for $p = p^I$:

$$p(r, z) = \sum_{n=0}^{M} P_n(r)\, Z_n(z; r). \tag{72}$$

The infinite system of o.d.e.'s (58) becomes accordingly, a $(M+1)\times(M+1)$ second-order o.d.e. system. This system is discretized using centered differences to approximate the derivatives of the functions $P_n(r)$, $n = 0, 1, 2, \ldots, M$. Discrete boundary conditions are also obtained by using appropriate differences to approximate derivatives in (63)–(66). The resulting discrete scheme is formally of second order in the horizontal direction.

Computing the coefficients a_{mn}, b_{mn}, c_{mn} of the system requires the evaluation of the local eigenfunctions $Z_n(z;r)$, $n \geq 1$, and their derivatives. In the general case, the latter would be obtained by *e.g.* solving the depth eigenvalue problem (29)–(33) by a second-order finite difference scheme, as described in Jensen *et al.*, [2]. In the simple case of our numerical experiments where c is piecewise constant, the vertical eigenfunctions are obtained analytically by the formulas (16)–(17) for $h_1 = h(r)$, $h_2 = H - h(r)$.

On the basis of the above considerations, we see that the coupled mode system of differential equations is finally reduced to a linear algebraic system. The coefficient matrix of the system is block structured (each block consisting of a tridiagonal matrix), and has a total size $N_d = (M+1)(N_s+1)$, where N_s is the number of segments in which the interval $[r_N, r_F]$ is subdivided. The forcing appears only at the left endpoint $r = r_N$; see Eq. (65). The linear system is solved by Gauss elimination using the built-in appropriate MATLAB function.

4 The Finite Element Method

We consider the homogeneous Helmholtz equation, *i.e.* (2) with zero right-hand side, on the domain $\Omega = \Omega_1 \cup \Omega_2 = \{(r,z) : R_1 \le r \le R_2,\ 0 \le z \le H\}$, where $0 < R_1 \le r_N$, $R_2 \ge r_F$, and Ω_1, Ω_2 represent the water and sediment layers, respectively. The equation is supplemented by the boundary conditions (3), (4), and the interface conditions (5), (6), while at the left-hand boundary $r = R_1$ we assume that

$$p(R_1, z) = g(z), \quad 0 \le z \le H, \tag{73}$$

where g is a known complex-valued function of z, given *e.g.* by the coupled mode program. At the right-hand (outflow) boundary $r = R_2$ we pose the exact, nonlocal, nonreflecting boundary condition

$$\frac{\partial p}{\partial r} = Tp, \quad r = R_2,\ 0 \le z \le H,$$

where T is the integral operator associated with the *Dirichlet-to-Neumann (DtN)* map of the exterior wave field evaluated at $r = R_2$, [15, 16, 17].

In order to construct T we use the far-field representation (10)

$$p^F(r,z) = \sum_{n=1}^{\infty} C_n^F\, Z_n^F(z)\, H_0^{(1)}\left(k_n^F r\right), \quad (r,z) \in D^F,$$

where $H_0^{(1)}$ is the Hankel function of the first kind and zero order and $(k_n^F)^2$, Z_n^F are the eigenvalues and eigenfunctions, respectively, of the two-point depth eigenvalue problem (11)–(15) with $* = F$. The eigenfunctions Z_n^F are assumed to be orthonormal with respect to the weighted L^2–inner product

$$(v,w)_\rho := \int_0^{h_F} v\overline{w}\, dz + \rho \int_{h_F}^{H} v\overline{w}\, dz, \quad \rho = \frac{\rho_1}{\rho_2}, \tag{74}$$

where an overbar denotes complex conjugation.

Then, the DtN map of the acoustic field in D^F, evaluated on $\{r = R_2,\ 0 \le z \le H\}$ is given by

$$\frac{\partial p(R_2,z)}{\partial r} = Tp(z) := \sum_{n=0}^{\infty} c_n(p)\, Z_n^F(z), \tag{75}$$

where

$$c_n(p) = k_n^F \frac{\sigma_n'}{\sigma_n} \left(p(R_2,\cdot), Z_n^F\right)_\rho, \quad \sigma_n' = \frac{dH_0^{(1)}}{dr}\left(k_n^F R_2\right), \quad \sigma_n = H_0^{(1)}\left(k_n^F R_2\right).$$

Now, let us denote $\Gamma_1 := \{(r,z) : R_1 \le r \le R_2,\ z = 0\}$, $\Gamma_2 := \{(r,z) : r = R_1,\ 0 \le z \le H\}$, $\Gamma_3 := \{(r,z) : R_1 \le r \le R_2,\ z = H\}$, $\Gamma_4 := \{(r,z) : r = R_2,\ 0 \le z \le H\}$. Let, also, $\overset{0}{\mathcal{H}}(\Omega, S)$ be the space of complex-valued functions u, defined on $\overline{\Omega}$, such that $\int_{\Omega_1} |u|^2 r\, dr dz + \rho \int_{\Omega_2} |u|^2 r\, dr dz < \infty$ and $\int_{\Omega_1} (|u_r|^2 + |u_z|^2) r\, dr dz + \rho \int_{\Omega_2} (|u_r|^2 + |u_z|^2) r\, dr dz < \infty$, and vanishing on a subset S of $\partial\Omega$. Then, the weak formulation of the above-mentioned boundary-value problem is the following: Seek $p \in \overset{0}{\mathcal{H}}(\Omega, \Gamma_1)$ satisfying $p = g$ on Γ_2 and

$$-(\nabla p, \nabla v)_{L^2_{1/2,\rho}(\Omega)} + (k^2 p, v)_{L^2_{1/2,\rho}(\Omega)} + (Tp, v)_{L^2_{1/2,\rho}(\Gamma_4)} = 0, \quad \forall\, v \in \overset{0}{\mathcal{H}}(\Omega, \Gamma_1 \cup \Gamma_2), \tag{76}$$

where the operator T is defined by (75), $\nabla = (\frac{\partial}{\partial r}, \frac{\partial}{\partial z})$, and

$$\begin{aligned}(u,v)_{L^2_{1/2,\rho}(\Omega)} &:= \int_{\Omega_1} u\overline{v}\, r dr dz + \rho \int_{\Omega_2} u\overline{v}\, r dr dz,\\ (u,v)_{L^2_{1/2,\rho}(\Gamma_4)} &:= \int_0^{h_F} u\overline{v}\, R_2 dz + \rho \int_{h_F}^{H} u\overline{v}\, R_2 dz.\end{aligned}$$

We shall assume that this boundary value problem has a unique solution.

4.1 The finite element discretization

The boundary-value problem given by (73), (76) is discretized by the standard Galerkin/finite element method with continuous in Ω, piecewise linear functions defined on a triangulation $\mathcal{T}_h$ of Ω with triangles of maximum sidelength h and nodes on the interface I_B. For simplicity, we assume that the interface consists of straight line segments; thus Ω_1 and Ω_2 are polygonal domains. We define the finite element spaces

$$\begin{aligned}S_h &= \{\phi:\ \phi \in C(\overline{\Omega}),\ \phi = 0 \text{ on } \Gamma_1,\ \phi\,|_\tau \in \mathbb{P}_1\ \ \forall\, \tau \in \mathcal{T}_h\},\\ S_h^0 &= \{\phi:\ \phi \in C(\overline{\Omega}),\ \phi = 0 \text{ on } \Gamma_1 \cup \Gamma_2,\ \phi\,|_\tau \in \mathbb{P}_1\ \ \forall\, \tau \in \mathcal{T}_h\}.\end{aligned}$$

Then S_h and S_h^0 are finite dimensional subspaces of $\overset{0}{\mathcal{H}}(\Omega, \Gamma_1)$ and $\overset{0}{\mathcal{H}}(\Omega, \Gamma_1 \cup \Gamma_4)$, respectively, and the discrete problem is formulated as follows: seek $p_h \in S_h$, such that $p_h\,|_{\Gamma_1} = \Pi_h g\,|_{\Gamma_1}$, and for every $\phi \in S_h^0$,

$$-(\nabla p_h, \nabla\phi)_{L^2_{1/2,\rho}(\Omega)} + (k^2 p_h, \phi)_{L^2_{1/2,\rho}(\Omega)} + (T_h p_h, \phi)_{L^2_{1/2,\rho}(\Gamma_4)} = 0. \tag{77}$$

Here $\Pi_h g$ is the piecewise linear interpolant of g on the grid induced by $\mathcal{T}_h$ on Γ_2, and T_h is a discrete approximation of T evaluated as a finite sum of all propagating and the most significant evanescent modes.

The error estimate for this discretization, proved by Goldstein, [16], in the case of homogeneous single-layer problems in Cartesian coordinates with a homogeneous Dirichlet boundary condition on Γ_3, was extended in [18], to the case of cylindrical coordinates for axisymmetric problems. If $T(p)$ is defined by (75), it is shown that the L^2 norm of the error $p - p_h$ is of $O(h^2)$. If the series in the right-hand side of (75) is truncated, so that the sum extends over all the propagating and sufficiently many of the evanescent modes, it may be shown that the H^1 norm of $p - p_h$ is of $O(h)$ plus a term of $O(\exp[-\frac{1}{2}|k_J^F|(R_2 - r_F)])$, where J is the order of the first evanescent term that is ignored. It is expected that a similar theory holds for the two-layer problem for solutions p that are smooth in each layer and satisfy the transmission conditions (5) and (6).

4.2 Implementation issues

The finite element method outlined above has been implemented in the Fortran code FENL; see [14] for a detailed description (*cf.* also http://www.hlsresearch.com/oalib/Other/fenl and the fenl.html file in the same site). Here we will just describe in brief the main ingredients of FENL.

1. To triangulate the domain Ω we use mesh generation techniques from the MODULEF library, [26], especially the modules APNOPO and TRIGEO. The generated mesh for range-varying interface topography is non-uniform. Hence, it is not possible to identify uniquely the number of meshpoints per wavelength, a parameter of practical interest in numerical simulations of wave propagation problems. Instead, we define an average meshlength parameter $\bar{h}_i := \sqrt{2|\Omega_i|/N_i}$, $i = 1$ or 2, where $|\Omega_i|$ denotes the area of Ω_i, and N_i the number of triangles in Ω_i. So, the number $\xi_i = c_i/(f\bar{h}_i)$, measures the number of (average size) meshlengths contained in a wavelength in the water ($i = 1$) or the sediment ($i = 2$), in the case of constant sound speeds c_i in the two media.

2. A subroutine is called which reads the MODULEF data structure and produces the information required for the assembly of the finite element matrices.

3. The next step is the numerical solution of the eigenvalue problem (11)–(15) with the standard Galerkin/finite element method with continuous, piecewise linear functions on the partition induced on $[0, H]$ by the triangulation $\mathcal{T}_h$. To solve it, we use routines from EISPACK.

4. We continue with the assembly of the stifness matrix S, the mass matrix Q, and the associated with the nonlocal condition on Γ_4 matrix B, with elements, respectively,

$$S_{ij} = (\nabla\phi_j, \nabla\phi_i)_{L^2_{1/2,\rho}(\Omega)}, \quad Q_{ij} = (k^2\phi_j, \phi_i)_{L^2_{1/2,\rho}(\Omega)}, \quad B_{ij} = (T_h\phi_j, \phi_i)_{L^2_{1/2,\rho}(\Gamma_4)},$$

   where ϕ_i, $i = 1, \ldots, N_h$ are the basis functions of the finite element space. S and Q are real, symmetric, sparse matrices, while B is complex symmetric.

5. The resulting linear system is large, sparse, indefinite and complex symmetric, and is solved with methods from the QMRPACK software package, [19]. QMPRPACK contains implementations of various Quasi-Minimal Residual (QMR) iterative algorithms. In the present work we have mainly used the double precision complex version of CPL (QMR based on coupled two-term look-ahead recurrences), combined with the two-sided SSOR preconditioner. A detailed experimental study of the influence of the various parameters of this class of iterative linear system solvers on the accuracy of the overall numerical method for underwater acoustics problems, such as the ones considered here, is contained in [18]. (See also [27]). Since most of the computational effort of the finite element method is devoted in solving the linear system, we report in the Appendix for each test problem of Section 5, the number of iterations required for convergence and the attendant CPU time.

6. Finally, to produce one- or two-dimensional transmission loss graphs we used MATLAB's PDE Toolbox, with the aid of a routine which exports the data (triangulation information and solution at the nodes) from FENL in the appropriate format needed by the graphics module.

5 Numerical Experiments

In this section we shall present the outcome of the numerical experiments that we performed with the aim of comparing FENL, CCMM and COUPLE in stratified environments with variable interface. (Extensive computations in the case of environments with a flat interface, have shown that the three codes provide results in perfect agreement with the analytical solution.) In this paper we shall confine ourselves to two problems, corresponding to interfaces that are shaped in the r,z plane like an underwater hill and an underwater trench with steep bathymetry and defined, respectively, by

$$h(r) = \begin{cases} 50 - 25\cos\frac{2\pi(r-500)}{400} & , \quad \text{for } 300 < r < 700, \\ 75 & , \quad \text{elsewhere,} \end{cases}$$

and

$$h(r) = \begin{cases} 65 + 25\cos\frac{2\pi(r-500)}{400} & , \quad \text{for } 300 < r < 700, \\ 40 & , \quad \text{elsewhere,} \end{cases}$$

where all distances are in meters. In all cases the density and sound speed of the seawater are taken constant and equal to $\rho_1 = 1.0$ g/cm^3, $c_1 = 1500$ m/sec, respectively; the density and sound speed of the sediment are $\rho_2 = 1.5$ g/cm^3 and $c_2 = 1700$ m/sec. The harmonic source is located at $z = 25$ m and the hard horizontal bottom was placed at $H = 100$ m. As a near field value on Γ_2 for the finite element method we took $\Pi_h g$, defined as the piecewise linear interpolant of the acoustic field produced by CCMM at $r = R_1$ on the grid induced by $\mathcal{T}_h$ on Γ_2. The nonlocal outflow condition for FENL was posed at $r = R_2$. In all cases CCMM used $r_N = 280$ m and $r_F = 720$ m. As linear system solver in FENL we selected CPL of QMRPACK, combined with the two-sided SSOR preconditioner with parameter $\omega = 1.2$. In all examples, we also compared our results with those obtained by COUPLE. (We have simulated the rigid bottom in COUPLE assuming that the semi-infinite layer used by COUPLE has very large values of density and sound speed.) We ran COUPLE, CCMM and FENL with parameters that are listed, for each test case, in the Appendix. In each case, the number of elements in FENL and the number of range steps in CCMM and COUPLE were taken sufficiently large so as to ensure convergent numerical results. In CCMM we chose M (*cf.* Eq. (72)) equal to 15, in order to guarantee that the number of evanescent modes retained in the representation of the field was greater than the number of propagating modes in all runs.

Test case 1: Hill, $f = 25$ Hz.

As a first example, we consider the case of the underwater hill for a frequency of f=25 Hz. In Figures 2 and 3 we present one- and two-dimensional transmission loss plots obtained by the CCMM, FENL and COUPLE codes.

In Figure 2 we show superimposed one-dimensional plots of transmission loss vs. range (at receiver depths RD=25, 50, 70 and 90 m) obtained by the three codes. The results are in excellent agreement. Table 1 contains some associated quantitative information. For a given pair

of codes, labeled, say, (1) and (2), and at each receiver depth z_{rd} we computed a 'normalized ℓ_2 field discrepancy', a measure of the difference between the two solutions $p^{(1)}(r, z_{rd})$ and $p^{(2)}(r, z_{rd})$, at the range points $Q \in \mathcal{Q}$, where $\mathcal{Q}$ is the set of the (equidistant) range nodes used by COUPLE in the interval $[R_1, R_2]$. (The values of R_1 and R_2 for each test case are listed in Table 7 in the Appendix.) The field values of FENL and CCMM were computed at the points Q by linear interpolation. The normalized ℓ_2 field discrepancy was defined as the quantity

$$\left(\frac{1}{J} \frac{\sum_{Q \in \mathcal{Q}} \left| p^{(1)}(Q, z_{rd}) - p^{(2)}(Q, z_{rd}) \right|^2}{\sum_{Q \in \mathcal{Q}} \left| p^{(1)}(Q, z_{rd}) \right|^2} \right)^{1/2},$$

where (2) denotes the code listed second in each indicated pair in the table and J is the number of interior sampling points Q in the interval $[R_1, R_2]$.

In Figure 3 we present two-dimensional transmission loss plots obtained by the three codes; the one-dimensional plots of Figure 2 were extracted from the runs that gave these 2D plots. □

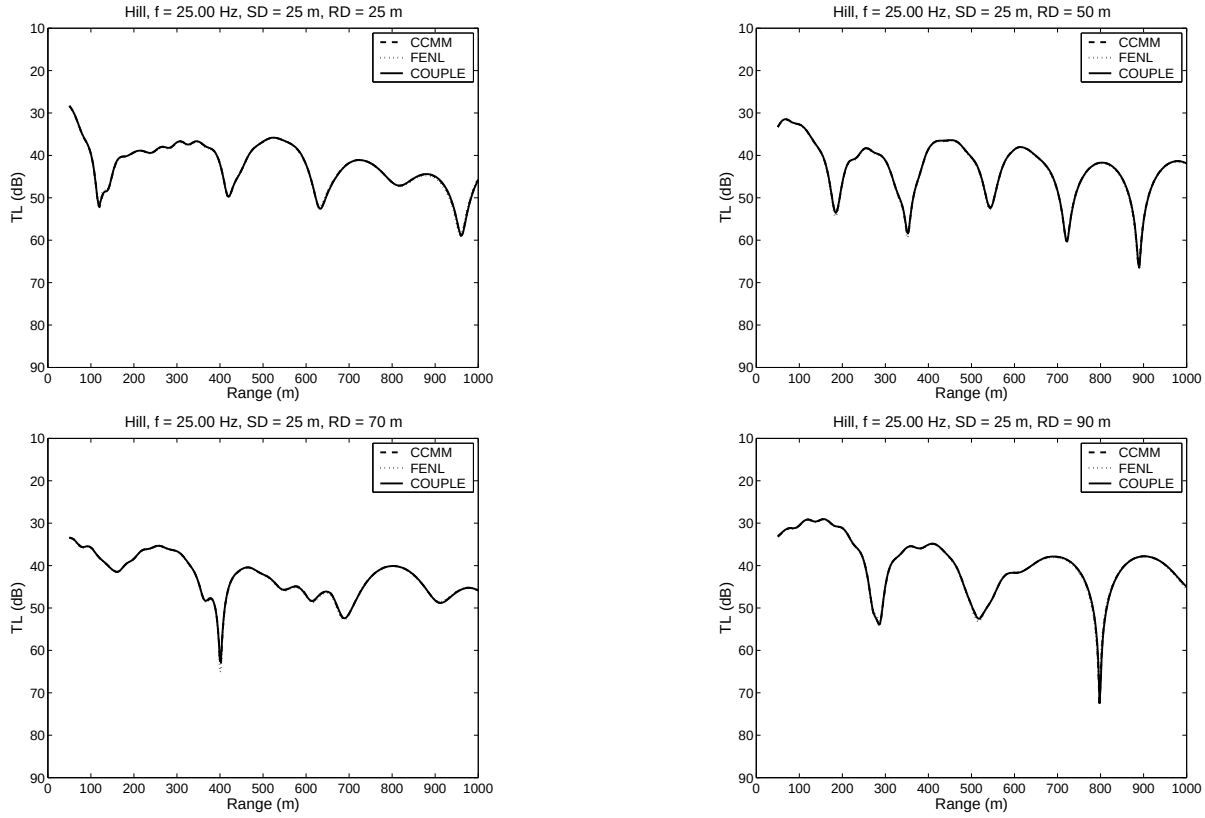

Figure 2: Underwater hill. Comparison between CCMM, FENL and COUPLE, f=25 Hz, R_1=50 m.

Depth (m)	CCMM vs. FENL	COUPLE vs. CCMM	COUPLE vs. FENL
25	7.8372E-04	2.6345E-04	8.5497E-04
50	7.9441E-04	2.2888E-04	8.0214E-04
70	6.4811E-04	2.7957E-04	6.0330E-04
90	7.8318E-04	2.4869E-04	8.0283E-04

Table 1: Normalized ℓ_2 field discrepancy, underwater hill, f=25 Hz, R_1=50 m.

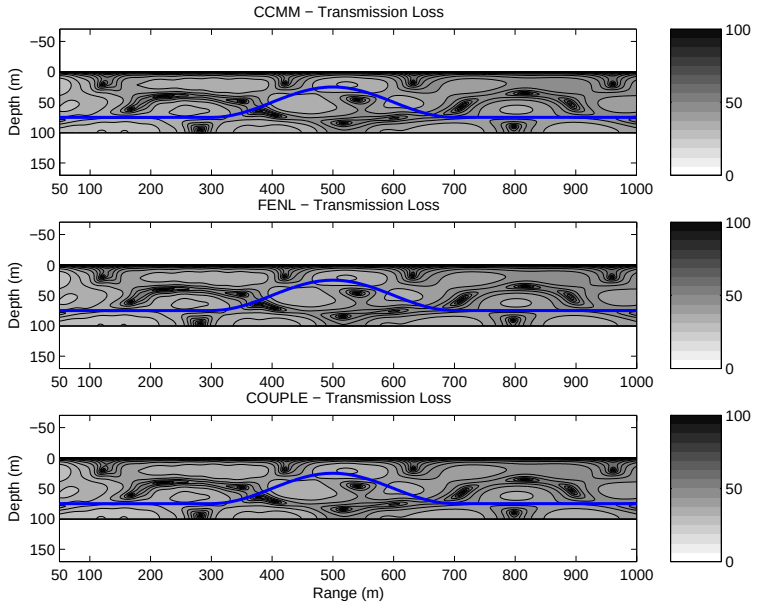

Figure 3: Underwater hill. Transmission loss. CCMM, FENL and COUPLE, f=25 Hz.

Test case 2: Trench, $f = 25$ Hz.

As a second example, we consider the case of the underwater trench for the frequency f=25 Hz. In Figure 4 we present two-dimensional transmission loss plots obtained by the three codes. The results again agree very well. In Figure 5 we plot superpositions of the transmission loss curves obtained by the three codes at receiver depths RD=25, 50, 70 and 90 m. Table 2 contains the associated normalized ℓ_2 field discrepancies between the pairs of methods, which are again of $O(10^{-4})$ like their counterparts of Table 1. □

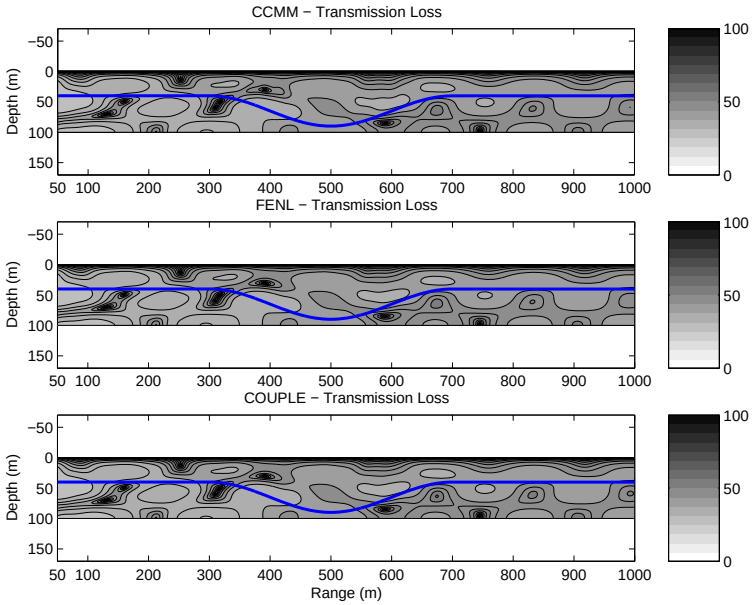

Figure 4: Underwater trench. Transmission loss. CCMM, FENL and COUPLE, f=25 Hz.

Depth (m)	CCMM vs. FENL	COUPLE vs. CCMM	COUPLE vs. FENL
25	6.7558E-04	6.1783E-04	4.5723E-04
50	5.3986E-04	4.2084E-04	5.6770E-04
70	4.3455E-04	3.7465E-04	5.1858E-04
90	4.4601E-04	2.8800E-04	5.4928E-04

Table 2: Normalized ℓ_2 field discrepancy, underwater trench, f=25 Hz, R_1=50 m.

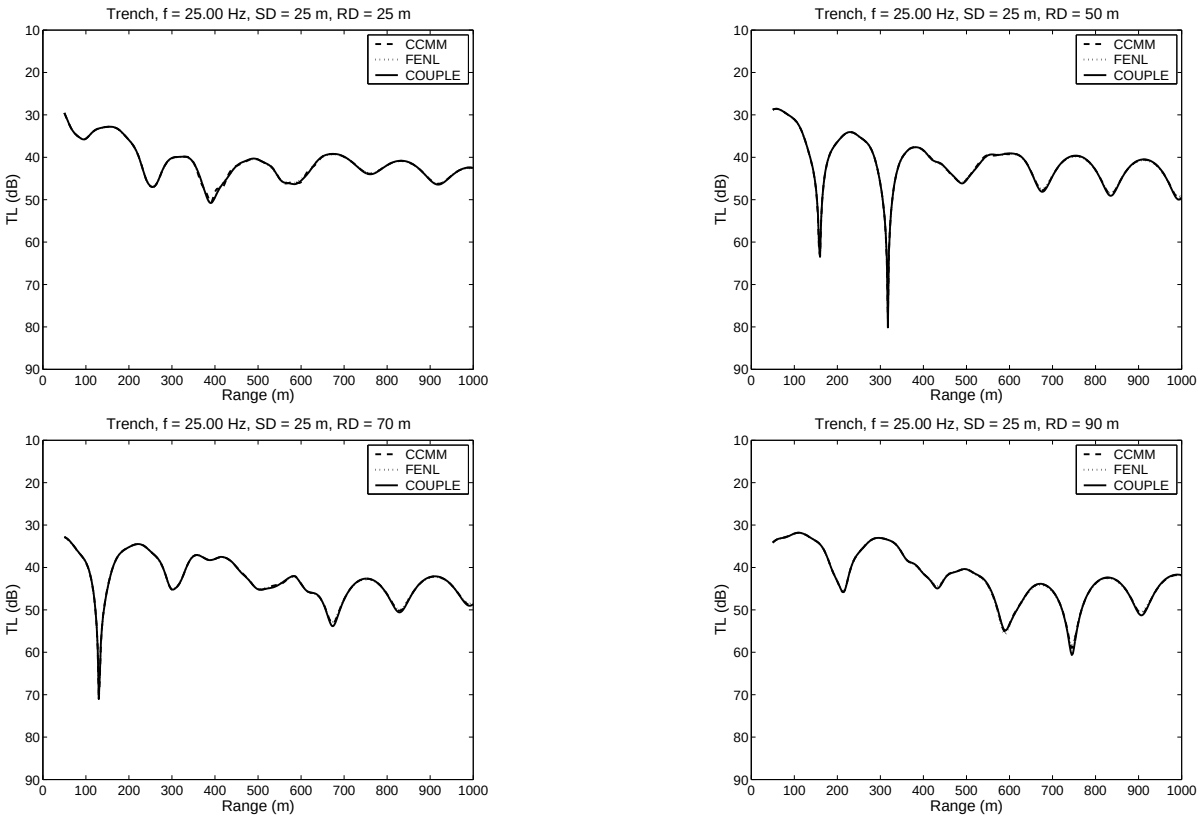

Figure 5: Underwater trench. Comparison between CCMM, FENL and COUPLE, f=25 Hz, R_1=50 m.

As was mentioned in the Introduction, we observed that there are values of the source frequency for which one eigenvalue $k_n^2(r)$ of the local vertical problem (29)-(33) remained close to zero for all r and changed sign, usually several times, in the vicinity of the hill or the trench. For example, for the hill case, in Figure 6 we have plotted as functions of r, for the three source frequencies f=25, 19.85, 27.75 Hz the three eigenvalues of the local vertical problem which are closer to zero, for $r \in [300, 700]$, *i.e.* when r ranges over the support of the hill (all distances in meters). The graphs are of course symmetric about $r = 500$, where the hill has its peak. (The eigenvalues were computed by considering the (interface) depth eigenvalue problem at $r = 300 + i\,\Delta r$, $i = 0, 1, 2, \ldots, 100$, $\Delta r = 4$, discretizing it by a finite element method with a meshlength equal to $\Delta z = 0.5$ in the depth variable, and solving the associated indefinite eigenvalue problem with EISPACK using the basic routine IMTQL2 for symmetric tridiagonal matrices.) When f=25 Hz the first three eigenvalues stay positive and the fourth is negative uniformly for $r \in [300, 700]$. In the case of the problematic frequency f=27.75 Hz the fourth eigenvalue changes sign six times in the interval, while for f=19.85 Hz the third eigenvalue after becoming negative for $r \simeq 380$, changes sign four times in the interval [450,550], where it is less than $7.\mathrm{E}-5$ in magnitude.

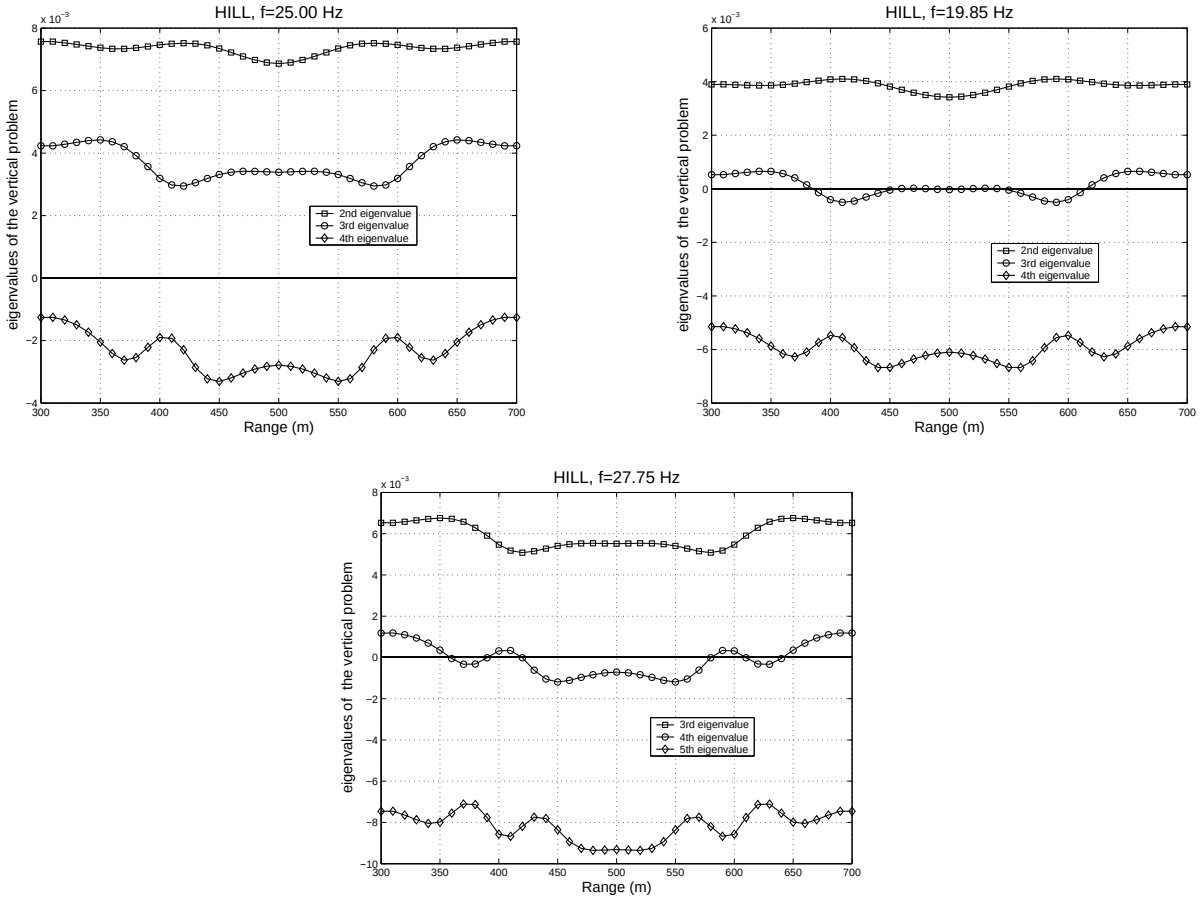

Figure 6: Some eigenvalues of the local, vertical problem as functions of r. Underwater hill, $f=$ 25.00 Hz, 19.85 Hz and 27.75 Hz

Let us first identify the first few 'critical' (multiple cut-off) frequencies for which this phenomenon occurs. There are actually *intervals* of critical frequencies, given, in the cases of the underwater hill and trench, in Table 3. The table indicates the mode number, *i.e.* the index n, of the problematic eigenvalue $k_n^2(r)$ which repeatedly crosses the zero line in the vicinity of the interface inhomogeneity. The endpoints of these intervals correspond to limiting profiles of

	Mode No.	3	4	5	6
Hill	Interval (Hz)	18.81 – 20.69	26.46 – 29.19	34.87 – 37.69	42.32 – 45.20
Trench	Interval (Hz)	18.81 – 20.69	26.31 – 28.22	33.81 – 36.68	41.31 – 44.89

Table 3: Intervals of critical frequencies, underwater hill and trench.

the corresponding eigenvalue, *i.e.* profiles that are just tangent, from below or above, to the zero line. For example, Figure 7 shows the graphs of the third eigenvalue of the hill problem at f=18.81 Hz and at f=20.69 Hz. For frequency values in the interval (18.81,20.69) the graph of the third eigenvalue will cross, therefore, the $\lambda = 0$ line at at least two points in the neighborhood

of the hill. The frequencies corresponding to the limiting profiles are found by solving Eq. (16)

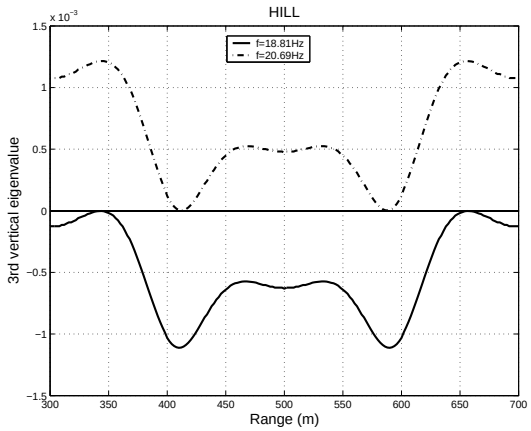

Figure 7: Underwater hill. Plots of $3^{\rm d}$ eigenvalue as function of r at the two endpoints of the first critical frequency interval.

for the unknown $f = \omega/(2\pi)$, using a standard root finder and putting $k_n = 0$. For example, in the case of the hill problem and $n = 3$, finite element eigenvalue calculations (such as the ones used to produce the profiles of Figure 6) yield the information that near the first set of critical frequencies, the minimum of $k_3^2(r)$ occurs at $r_{\rm min} \cong 412$ m, corresponding to an interface depth $h(r_{\rm min}) = 45.315$ m, while the maximum occurs at $r_{\rm max} \cong 344$ m, where $h(r_{\rm max}) = 69.263$ m. Using $h_* = h(r_{\rm max})$ in (16) yields the lower critical frequency endpoint $f \cong 18.81$ Hz, while if $h_* = h(r_{\rm min})$ the root of (16) is $f \cong 20.69$ Hz, the upper limit of the critical frequency interval for $n = 3$.

We now examine in detail the results that the three codes gave at some critical frequencies.

Test case 3: Hill, $f = 19.85$ Hz.

In this case, we obtained the transmission loss vs. range curves of Figure 8, showing superimposed plots derived from output from the three codes CCMM, FENL and COUPLE at four receiver depths, $RD = 25$, 50, 70 and 90 meters. The agreement is quite good as it is evident in the graphs, and is quantified by means of the associated ℓ_2 field discrepancy data of Table 4. Note that its entries have larger magnitudes compared with their counterparts of Table 1. For example, the discrepancies between the CCMM and COUPLE results have increased by a factor of about five. The differences between the CCMM or COUPLE and FENL codes have also increased. □

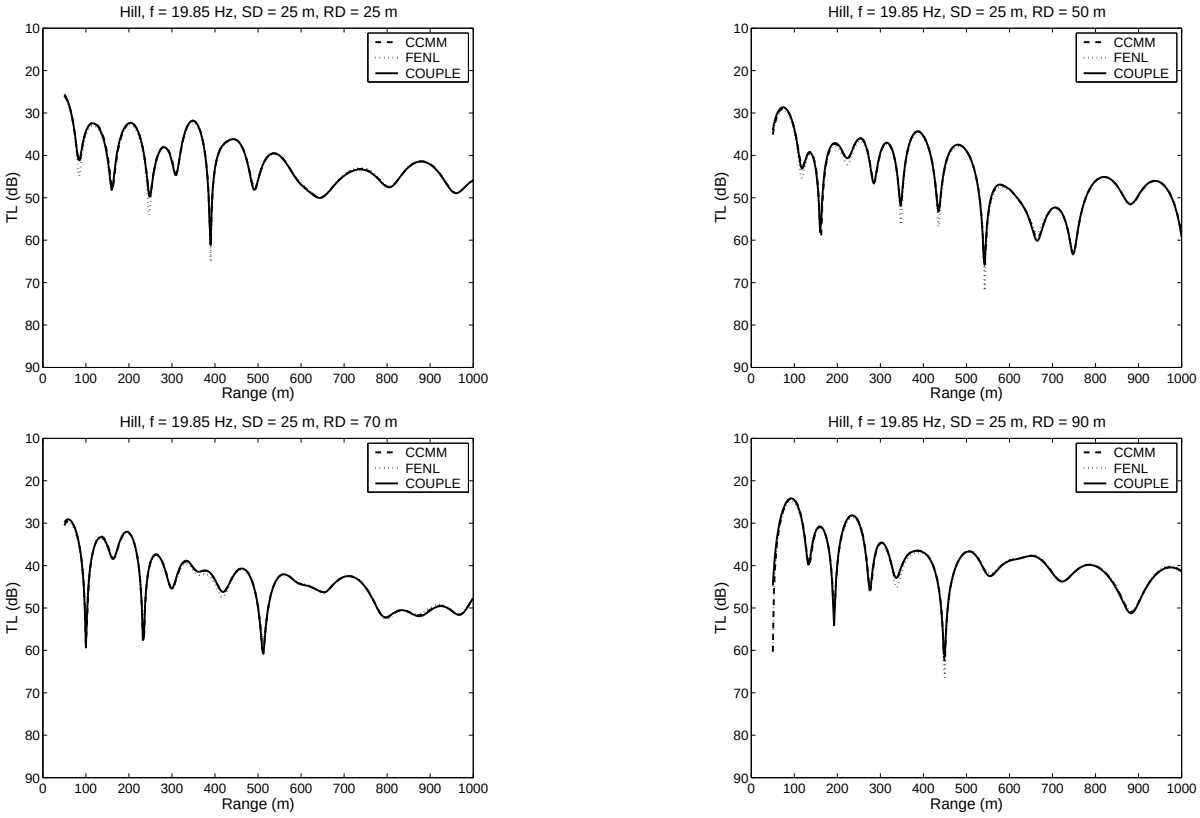

Figure 8: Underwater hill. Comparison between CCMM, FENL and COUPLE, f=19.85 Hz, R_1=50 m.

Depth (m)	CCMM vs. FENL	CCMM vs. COUPLE	COUPLE vs. FENL
25	2.8871E-03	1.2651E-03	3.0139E-03
50	3.2783E-03	1.7551E-03	3.7983E-03
70	2.1468E-03	1.3498E-03	2.5490E-03
90	3.0089E-03	1.8694E-03	3.4218E-03

Table 4: Normalized ℓ_2 field discrepancy, underwater hill, f=19.85 Hz, R_1=50 m.

Test case 4: Hill, $f = 27.75$ Hz.

Figure 9 presents superimposed transmission loss plots obtained by the three codes. The results agree quite well, but once more, as it is verified by examining the entries of the associated Table 5, the discrepancies are larger compared with those of Table 1. □

We turn now to the problem of the underwater trench. The general picture that emerges is similar to that of the underwater hill. As it has been seen already, the value f=25 Hz (Test Case

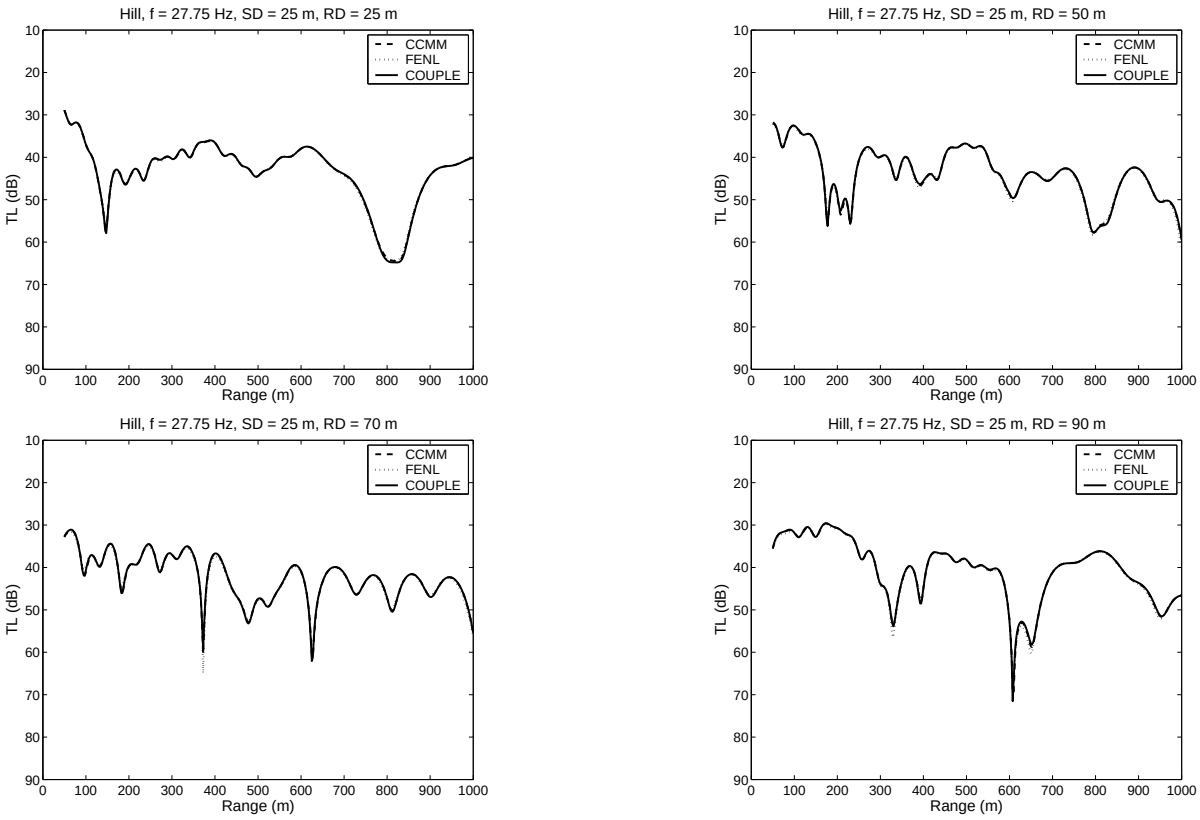

Figure 9: Underwater hill. Comparison between CCMM, FENL and COUPLE, f=27.75 Hz, R_1=50 m.

2) was a frequency for which we observed good agreement between the three codes. We next examine the case of the frequency 19.65 Hz, a value in the first interval of critical frequencies for the trench.

Test case 5: Trench, $f = 19.65$ Hz.

In this case, Figure 10 shows the transmission loss vs. range curves that we have obtained from the three codes. The agreement is now slightly worse and is quantified by the data of Table 6 presenting the associated normalized ℓ_2 field discrepancies; its entries have increased in comparison with their counterparts of Table 2. Figure 11 is the analogous of Figure 6 for the trench example at f=25 and 19.65 Hz. □

We close this section with some remarks regarding the near-field boundary condition (on Γ_2, for $r = R_1$) needed by the finite element code FENL. This boundary condition is furnished (unless otherwise specified) by the CCMM solution at $r = R_1$; R_1 was always taken greater or equal to 50 m so as not to be too close to the source. We observed that varying R_1 gave, in general, different discrepancies between FENL and the coupled mode codes. Figure 12 summarizes the FENL-CCMM comparison results in the hill case. It shows the normalized l_2 field

Depth (m)	CCMM vs. FENL	COUPLE vs. CCMM	COUPLE vs. FENL
25	9.2522E-04	3.9439E-04	9.5602E-04
50	1.6352E-03	5.5933E-04	1.6915E-03
70	2.4457E-03	6.7366E-04	2.5661E-03
90	1.2330E-03	4.6935E-04	1.3481E-03

Table 5: Normalized ℓ_2 field discrepancy, underwater hill, f=27.75 Hz, R_1=50 m.

Depth (m)	CCMM vs. FENL	COUPLE vs. CCMM	COUPLE vs. FENL
25	8.9033E-03	1.7573E-03	7.9856E-03
50	7.9446E-03	1.2474E-03	7.5068E-03
70	6.4461E-03	1.3418E-03	5.7600E-03
90	8.8960E-03	1.4641E-03	8.1229E-03

Table 6: Normalized ℓ_2 field discrepancy, underwater trench, f=19.65 Hz, R_1=50 m.

discrepancy at four receiver depths for various source frequencies as a function of six positions R_1, the smaller of which was 50 m and the larger 280 m. In the case (a) of the 'regular' frequency f=25 Hz the results are insensitive to R_1. But at critical frequencies such as 19.85 Hz, (b), and 27.75 Hz, (c), we observe stronger dependence of the discrepancies on R_1. The discrepancies are apparently caused by the quality of the modal boundary data or, perhaps, by the possible inappropriateness of the Dirichlet data at these range values that leads to some type of resonance between the near-field boundary data and the inhomogeneity. They are not due, for example, to some inherent FENL instability with respect to variations in R_1: When we took near-field data from CCMM at R_1=50 m, computed the solution by FENL at r=100, 150, 200, 250 and 280 m and used these values as boundary conditions for FENL at these R_1's, we observed (Figure 12(d)) discrepancies that are independent of R_1 and much smaller than those of case (c). We observed a similar R_1-dependence when we took modal data for FENL from COUPLE. However, the discrepancies depend on the particular modal starter used. For example, for the frequency f= 19.85 Hz, in Figure 13(a) we show the resulting transmission loss vs. range curves for CCMM and FENL at receiver depth 90 m, when modal data from CCMM was used as boundary condition for FENL at R_1=150 m. (From Figure 12(b) we see that this is the worst-case scenario with respect to the choice of R_1 and receiver depth at this critical frequency.) The associated normalized ℓ_2 field discrepancy is 1.41E-2. When we used the COUPLE field values at R_1=150 m as boundary data for FENL, we obtained much better agreement, *cf.* Figure 13(b). The ℓ_2 discrepancy is now 2.09E-3.

Figure 14 shows analogous graphs of the dependence on R_1 of the discrepancy between the FENL and CCMM fields when the FENL boundary condition at R_1 is furnished by CCMM, in the case of a regular (f=25 Hz) and a critical (f=19.65 Hz) frequency for the trench problem.

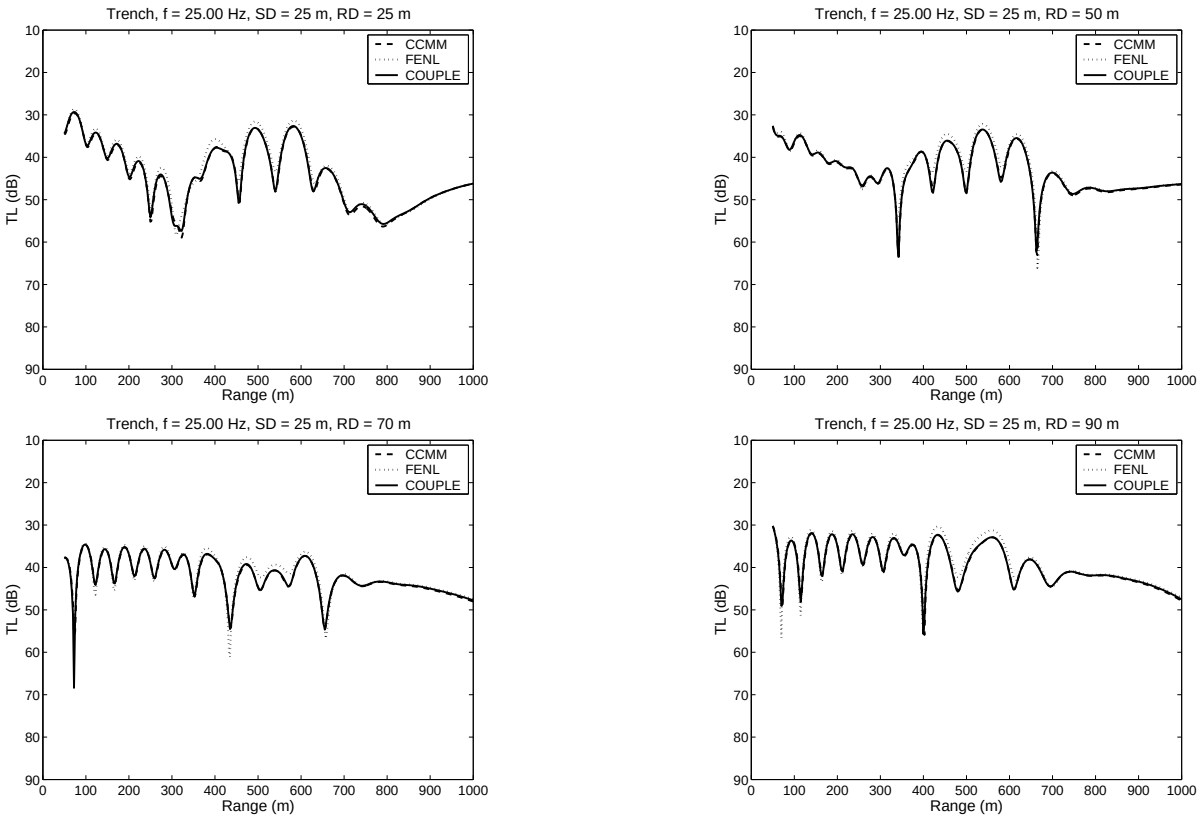

Figure 10: Underwater trench. Comparison between CCMM, FENL and COUPLE, f=19.65 Hz, R_1=50 m.

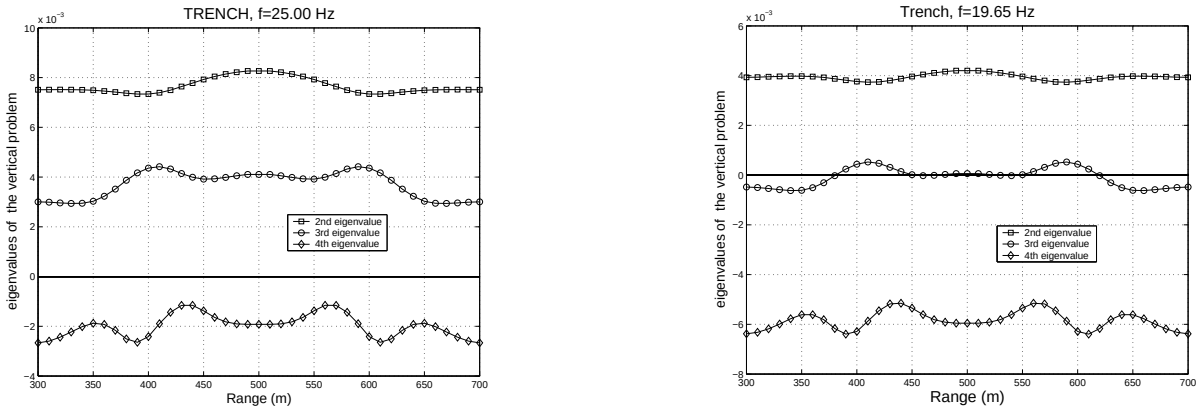

Figure 11: Some eigenvalues of the vertical problem as functions of r. Underwater trench, $f=$ 25.00 Hz, 19.65 Hz.

6 Concluding Remarks

In this paper we solved a standard underwater acoustic propagation and scattering problem in two cylindrically symmetric, range-dependent, shallow-water ideal environments consisting of the water and one sediment layer separated by a hill– and a trench–like interface and overlying a rigid bottom at finite depth. We used the coupled mode method CCMM and the finite element method FENL, and compared their results for various relatively low values of the source frequency, in order to keep the number of elements of the finite element scheme at reasonable levels as required by our version of Fortran implementation of MODULEF. In all cases we also compared the results of these two codes with those of COUPLE.

The Consistent Coupled Mode Method (CCMM) uses an enhanced local-mode representation of the pressure field in an intermediate domain that contains the variable topography part of the water-sediment interface. The modal expansion includes an additional local field element, the 'sloping interface mode', whose range-dependent coefficient provides an additional degree of freedom, that is used to correct the inconsistency of the local modes, which satisfy the derivative jump condition not in the normal direction to the interface as dictated by the problem, but only in the vertical direction. This, in turn, significantly accelerates the convergence of the modal series. The intermediate field is then matched with the standard near-field and far-field (outgoing) series solutions in the respective, homogeneous parts of the waveguide. The finite element method FENL solves the Helmholtz equation in a computational domain that includes the variable topography part of the interface and is bounded by inner and outer vertical cylindrical boundary surfaces of radii $r = R_1$ and $r = R_2$, respectively. FENL employs continuous piecewise linear functions defined on a triangulation of the computational domain, and the standard Galerkin approximation coupled with a nonlocal, nonreflecting DtN-type boundary condition at the outer boundary $r = R_2$. At the inner (inflow) boundary $r = R_1$ FENL uses as a Dirichlet boundary condition the value of the pressure field that is computed by modal data

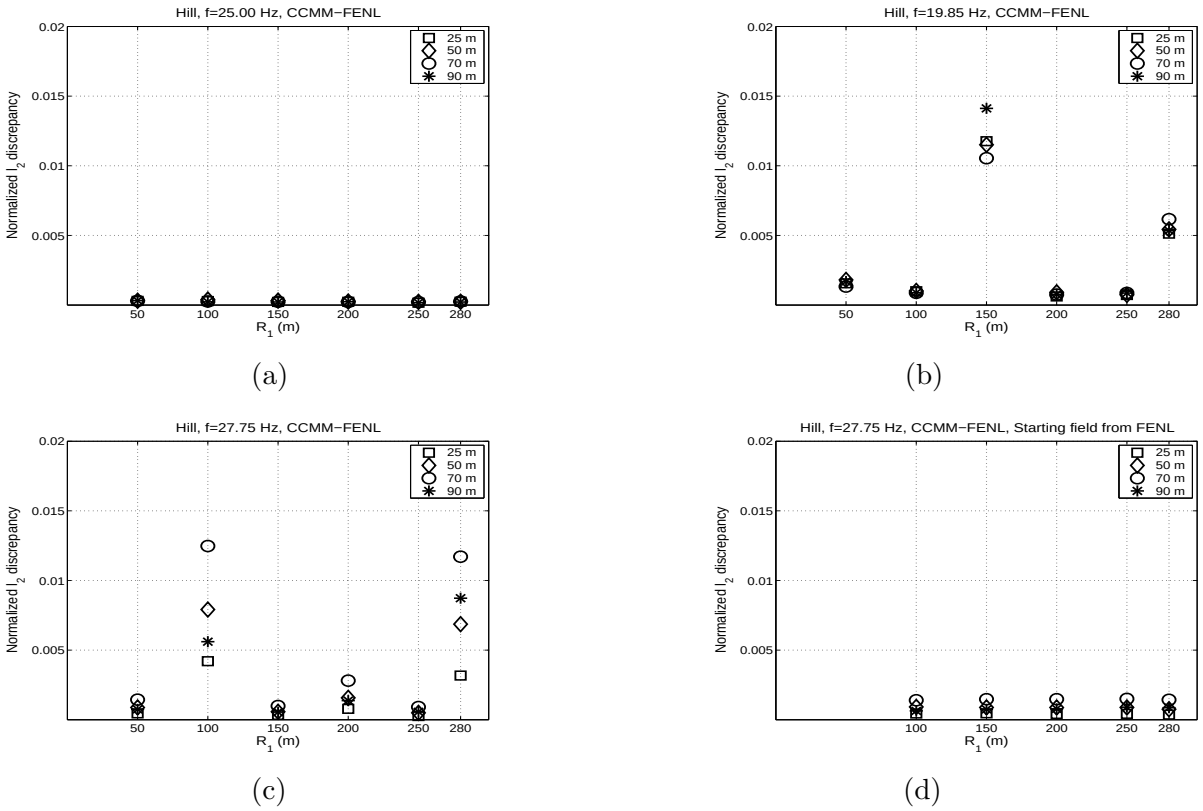

Figure 12: Underwater hill. Influence of the position R_1 of the FENL near-field boundary on the normalized ℓ_2 discrepancy between FENL and CCMM, f=25 Hz, 19.85 Hz, and 27.75 Hz, RD = 25, 50, 70, and 90 m.

(usually provided by CCMM) at $r = R_1$ for the particular problem. Thus, the results of a FENL computation depend, through the boundary condition at the inner boundary, on the results of the corresponding modal calculation. (It is possible to make FENL self-contained by coupling the main solver with a nonhomogeneous DtN–type condition at the inner boundary using the near field expansion of the solution at $r = R_1$; this will be pursued in the future.)

We compared the results of the three codes in some detail, providing in each test case superimposed one-dimensional transmission loss plots at various depths, as well as quantitative evidence of the ℓ^2 norm of the discrepancies of the fields computed by the three pairs of codes. Thus, our data might prove useful in comparing the results of other codes on these two test problems. In general, the results of the three codes were in very good agreement. Larger discrepancies were observed for source frequencies that were such that one eigenvalue $k_n^2(r)$ of the local, vertical problem (29)–(33) remained small in magnitude and changed sign, usually several times, in the neighborhood of the hill or trench. Examples of such 'critical' frequencies and descriptions of the associated differences in the results of the codes may be found in Section 5 (Test Cases 3–5). In all cases the dicrepancies were small in absolute terms, with the exception of cases corresponding to 'resonant' values of R_1 as discussed in the end of Section 5.

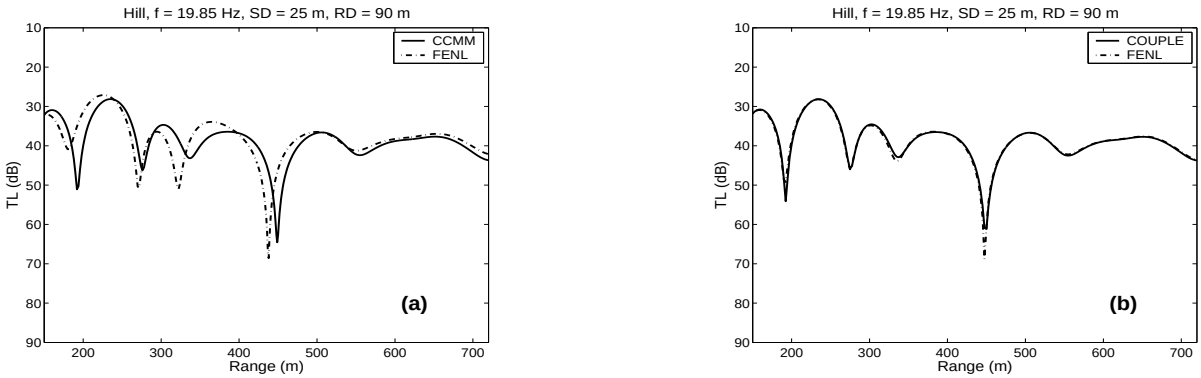

Figure 13: Underwater hill. Influence of (a) CCMM and (b) COUPLE data at R_1=150 m, f=19.85 Hz.

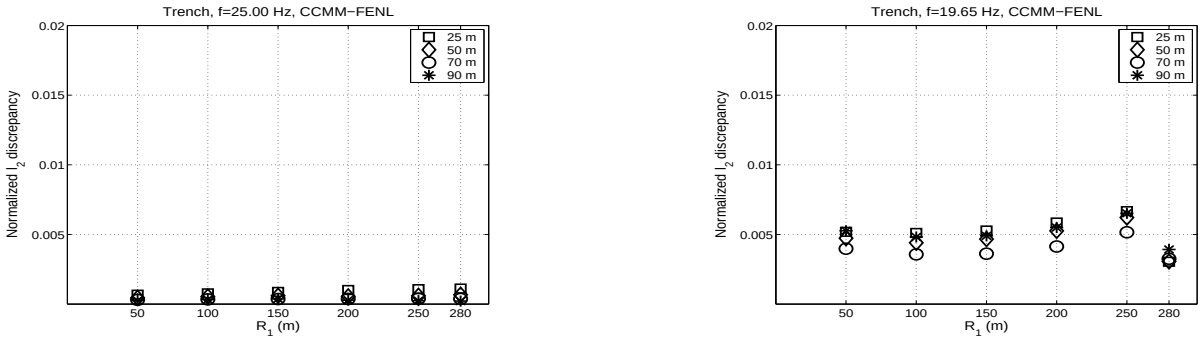

Figure 14: Underwater trench. Influence of the position R_1 of the near-field boundary on the normalized ℓ_2 field discrepancy between FENL and CCMM, f=25 Hz and 19.65 Hz, RD = 25, 50, 70, and 90 m.

Coupled mode codes depend, of course, explicitly on computed local eigenfunctions and eigenvalues of the depth problem. Evidence from our experiments (*cf.* Test Case 3 (Table 4), Test Case 4 (Table 5) and Test Case 5 (Table 6)) shows that relatively larger discrepancies between the CCMM and COUPLE results may be observed at critical frequencies in both the hill and the trench examples. This may be due to some kind of mild numerical instability that influences the accuracy of coupled mode schemes in the presence of such 'blurred' eigenvalues in the course of computing the associated modal amplitude functions.

As pointed out in the Introduction, for a locally flat interface one may expect problems in computing the modal amplitude functions $P_n(r)$. In the case of COUPLE, which uses piecewise constant approximations to the interface, k_n is never actually zero because of a heuristic check of the code that slightly modifies the interface depth near such ranges. More importantly, COUPLE uses a halfspace bottom approximation which effectively pushes the eigenvalues that are close to zero, into the complex plane. CCMM does not have such explicit perturbation mechanisms in place; apparently, including the sloping interface mode amplitude $P_0(r)$ in the system of o.d.e's

(58), and truncating and discretizing this system by finite differences introduce some type of regularization into the problem. We observed that the condition number of the matrix of the linear system that is solved in CCMM (*cf.* end of Section 3.5) typically increases by a factor of 10 near some critical frequencies. This increase is not large enough to cause serious loss of accuracy.

The finite element method does not explicitly require computing the solution of the local depth eigenvalue problem. (The FENL code includes, of course, such a computation but only at the outflow boundary $r = R_2$ for the implementation of the nonlocal, DtN type boundary condition; however that eigenvalue problem involves only the eigenpairs $\left\{ \left(k_n^F\right)^2, Z_n^F \right\}$ of the far field, which are independent of r.) However, as previously stated, in these numerical experiments the boundary condition required by FENL at the inflow boundary is provided by the field value at $r = R_1$ that is computed by a coupled mode code. Thus, the accuracy of a FENL computation is influenced by the accuracy of the analogous modal computation and, as seen in Section 5, depends in general on the position of R_1.

Acknowledgments

The authors would like to thank two unnamed referees of the first version of the paper for their criticisms and suggestions. Mitsoudis and Dougalis would like to gratefully acknowledge partial support for this research from a "Pythagoras"–O.P.Education grant to the University of Athens, funded by the Ministry of National Education, Greece, and the European Union (European Social Fund).

References

[1] R. B. Evans, *COUPLE: A user's manual*, NORDA TN–332 (1986).

[2] F. Jensen, W. Kupperman, M. Porter and H. Schmidt, *Computational Ocean Acoustics*, (AIP Press, 1994).

[3] C. Allan Boyles, *Acoustic Waveguides: Applications to Oceanic Science*, (Wiley, 1984).

[4] A. D. Pierce, Extension of the method of normal-modes to sound propagation in an almost stratified medium, *J. Acoust. Soc. Am.* **37**, 19–27 (1965).

[5] A. D. Pierce, Augmented adiabatic mode theory for upslope propagation from a point source in a variable-depth shallow water overlying a fluid bottom, *J. Acoust. Soc. Am.* **74**, 1837–1847 (1983).

[6] R. B. Evans, A coupled mode solution for the acoustic propagation in a waveguide with stepwise depth variations of a penetrable bottom, *J. Acoust. Soc. Am.* **74**, 188–195 (1983).

[7] S. R. Rutherford and K. E. Hawker, Consistent coupled mode theory of sound propagation for a class of nonseparable problems,*J. Acoust. Soc. Am.* **70**, 554–564 (1981).

[8] L. M. Brekhovskikh and O.A. Godin, *Acoustics of Layered Media. 2: Point Sources and Bounded Beams*, Springer Series on Wave Phenomena Vol. 10 (Springer-Verlag, Berlin, 1992).

[9] J. A. Fawcett, A derivation of the differential equations of coupled mode propagation, *J. Acoust. Soc. Am.* **97**, 290–295 (1992).

[10] C.-S. Chiu, J. H. Miller and J. F. Lynch, Forward coupled-mode propagation modeling for coastal acoustic tomography, *J. Acoust. Soc. Am.* **99**, 793–802 (1996).

[11] O. A. Godin, A note on differential equations of coupled mode propagation in fluids, *J. Acoust. Soc. Am.* **103**, 159–168 (1998).

[12] G.A. Athanassoulis, K. A. Belibassakis, "Rapidly-convergent local-mode representations for wave propagation and scattering in curved-boundary waveguides", in *Proc. 6^{th} International Conference on Mathematical and Numerical Aspects of Wave Propagation (Waves 2003)*, G. C. Cohen. E. Heikkola, P. Joly, P. Neittaanmäki eds., Springer, 2003, pp. 451–456.

[13] M. J. Buckingham, Ocean-acoustic propagation models, *J. Acoustique* **3**, 223–287 (1992).

[14] N. A. Kampanis, V. A. Dougalis, A finite element code for the numerical solution of the Helmholtz equation in axially symmetric waveguides with interfaces, *J. Comp. Acoustics* **7**, 83–110 (1999).

[15] G. J. Fix, S. P. Marin, Variational methods for underwater acoustic problems, *J. Comp. Physics* **28**, 253–270 (1978).

[16] C. I. Goldstein, A finite element method for solving Helmholtz type equations in waveguides and other unbounded domains, *Math. Comp.* **39**, 309–324 (1982).

[17] J. B. Keller, D. Givoli, Exact nonreflecting boundary conditions, *J. Comp. Physics* **82**, 172–192 (1989).

[18] D. A. Mitsoudis, Finite element methods for axisymmetric, indefinite boundary-value problems and applications in underwater acoustics (in Greek), Ph.D. Thesis, University of Athens, Greece, 2003.

[19] R. W. Freund, N. M. Nachtigal, An implementation of the QMR method based on coupled two–term recurrences, *SIAM J. Sci. Comput.* **15**, 313–337 (1994).

[20] M. J. Buckingham, A. Tolstoy, An analytical solution for benchmark problem 1: The "ideal" wedge, *J. Acoust. Soc. Am.* **88**, 1511–1513 (1990).

[21] V. A. Dougalis, N. A. Kampanis, M. I. Taroudakis, "Comparison of finite element and coupled mode solutions of the Helmholtz equation in underwater acoustics", in *Proc. 4th European Conference in Underwater Acoustics*, eds. A. Alippi and G. B. Cannelli, CNR-IDAC, Rome 1998, Vol. II, pp. 649–654.

[22] M. I. Taroudakis, G. A. Athanassoulis, and J. P. Ioannidis, A variational principle for underwater acoustic propagation in a three-dimensional ocean environment, *J. Acoust. Soc. Am.* **88**, 1515–1521 (1990).

[23] M. I. Taroudakis, G. A. Athanassoulis, and J. P. Ioannidis, A hybrid solution of the Helmholtz equation in shallow water, based on a variational principle, in *Acoustique Sous Marine et Ultrasons*, CNRS–LMA, Marseilles 1991, pp. 213–227.

[24] I. M. Gelfand and S. V. Fomin, *Calculus of variations* (Prentice Hall, 1962).

[25] K. Rectorys, *Variational Methods in Mathematics. Science and Engineering*, (D. Reidel, 1977).

[26] M. Bernadou, P. L. George, A. Hassim, P. Joly, P. Laug, A. Perronnet, E. Saltel, D. Steer, G. Vanderborck and M. Vidrascu, *MODULEF: A Modular Library of Finite Elements*, INRIA, 1988.

[27] D. A. Mitsoudis, N. A. Kampanis, V. A. Dougalis, "A finite element method for the Helmholtz equation in axially symmetric problems of underwater acoustics: error estimates and numerical experiments", in *Proc. 5th Hellenic-European Conference on Computer Mathematics and its Applications (HERCMA 2001)*, E. A. Lipitakis ed., (Athens, Greece, 2001), pp. 530–533.

A Appendix

In Table 7 we list the parameters used in the FENL code in the various experiments of Section 5. (All distances in meters). For CCMM we used 441 (equidistant) nodes in range between $r_N = 280$ and $r_F = 720$, and we chose M (*cf.* Eq. (72)) equal to 15, for all test cases. For COUPLE we used NI=400 regions in range between $r = 300$ and $r = 700$, and 15 contributing modes. In COUPLE, we simulated the hard bottom by a bottom layer of density 10^9 g/cm^3 and sound speed 10^9 m/sec. For FENL, R_1 is the range value where the near-field boundary data was evaluated, R_2 is the range value where the DtN condition was posed, NEL is the number of elements and NND is the number of nodes of the triangular mesh, ξ_i is an indicative parameter measuring the number of average size meshlengths contained in a wavelength in the water ($i = 1$) or the sediment ($i = 2$), for constant sound speeds $c_1 = 1500$ m/sec and $c_2 = 1700$ m/sec in the two media. The parameter NIT is the number of iterations that the linear system solver requires to converge and t is the linear system solve total CPU-time in seconds. (All the FENL

runs were performed on a Pentium IV PC with a RAM of 1 GB running under Linux at 2 GHz.)

		FENL							
Cases		R_1	R_2	NEL	NND	ξ_1	ξ_2	NIT	t
TC1 Hill 25 Hz	Fig. 2, Fig. 3, Tbl. 1	50	1000	53,142	27,087	32	36	1,045	66
TC2 Trench 25 Hz	Fig. 4, Fig. 5, Tbl. 2	50	1000	53,352	27,203	32	36	1,299	83
TC3 Hill 19.85 Hz	Fig. 8, Tbl. 4	50	1000	53,142	27,087	40	45	1,014	64
TC4 Hill 27.75 Hz	Fig. 9, Tbl. 5	50	1000	53,142	27,087	29	32	1,415	89
TC5 Trench 19.65 Hz	Fig. 10, Tbl. 6	50	1000	53,352	27,203	40	46	1,200	77

Table 7: FENL run parameters for the numerical experiments of Section 5.